Did a submarine landslide contribute to the 2011 Tohoku tsunami?

CrossMark

David R. Tappin [a,*], Stephan T. Grilli [b], Jeffrey C. Harris [b,1], Robert J. Geller [c], Timothy Masterlark [d], James T. Kirby [e], Fengyan Shi [e], Gangfeng Ma [f], K.K.S. Thingbaijam [g], P. Martin Mai [g]

[a] British Geological Survey, Keyworth, Nottingham, UK
[b] Department of Ocean Engineering, University of Rhode Island, Narragansett, RI, USA
[c] Department of Earth and Planetary Science, Graduate School of Science, University of Tokyo, Tokyo, Japan
[d] Department of Geology and Geological Engineering, South Dakota School of Mines and Technology, Rapid City, SD, USA
[e] Center for Applied Coastal Research, University of Delaware, Newark, DE, USA
[f] Department of Civil and Environmental Engineering, Old Dominion University, Norfolk, VA, USA
[g] Division of Physical Sciences and Engineering, King Abdullah University of Science and Technology, Thuwal, Saudi Arabia

ARTICLE INFO

ABSTRACT

Many studies have modeled the Tohoku tsunami of March 11, 2011 as being due entirely to slip on an earthquake fault, but the following discrepancies suggest that further research is warranted. (1) Published models of tsunami propagation and coastal impact underpredict the observed runup heights of up to 40 m measured along the coast of the Sanriku district in the northeast part of Honshu Island. (2) Published models cannot reproduce the timing and high-frequency content of tsunami waves recorded at three nearshore buoys off Sanriku, nor the timing and dispersion properties of the waveforms at offshore DART buoy #21418. (3) The rupture centroids obtained by tsunami inversions are biased about 60 km NNE of that obtained by the Global CMT Project.

Based on an analysis of seismic and geodetic data, together with recorded tsunami waveforms, we propose that, while the primary source of the tsunami was the vertical displacement of the seafloor due to the earthquake, an additional tsunami source is also required. We infer the location of the proposed additional source based on an analysis of the travel times of higher-frequency tsunami waves observed at nearshore buoys. We further propose that the most likely additional tsunami source was a submarine mass failure (SMF—i.e., a submarine landslide). A comparison of pre- and post-tsunami bathymetric surveys reveals tens of meters of vertical seafloor movement at the proposed SMF location, and a slope stability analysis confirms that the horizontal acceleration from the earthquake was sufficient to trigger an SMF. Forward modeling of the tsunami generated by a combination of the earthquake and the SMF reproduces the recorded on-, near- and offshore tsunami observations well, particularly the high-frequency component of the tsunami waves off Sanriku, which were not well simulated by previous models. The conclusion that a significant part of the 2011 Tohoku tsunami was generated by an SMF source has important implications for estimates of tsunami hazard in the Tohoku region as well as in other tectonically similar regions.

1. Introduction

The March 11th, 2011 Tohoku earthquake, which struck northeast Japan at 2:46 pm JST, is the largest instrumentally recorded Japanese earthquake and one of the world's largest. This extremely large, shallow subduction zone event (Fig. 1) caused a highly destructive tsunami, which devastated the Pacific coast of the Tohoku region between 35°–43° N. The most recent data published by Japan's National Police Agency (as of August 8, 2014) show that 18,490 people died (including the missing) (http://www.npa.go.jp/archive/keibi/biki/index_e.htm). South of 38° 30′ N tsunami runups were up to 20 m, with 10–15 m recorded on the low-lying Sendai Plain (Mori et al., 2012; see figure at http://www.coastal.jp/ttjt/index.php?plugin=ref&page=FrontPage&src=surveyge.jpg). Larger wave activity was focused farther to the north, on the coast of the Sanriku district between 38° 30′ N and 40° 30′ N (Fig. 1b and web link above), where tsunami waves were highest, with peak flow depths and runups of 40 m. Because the Tohoku earthquake was an extremely

* Corresponding author.
  E-mail addresses: drta@bgs.ac.uk (D.R. Tappin), grilli@oce.uri.edu (S.T. Grilli),
jharris@egr.uri.edu (J.C. Harris), bob@eps.s.u-tokyo.ac.jp (R.J. Geller),
Timothy.Masterlark@sdsmt.edu (T. Masterlark), kirby@udel.edu (J.T. Kirby),
fyshi@udel.edu (F. Shi), gma@odu.edu (G. Ma), k.thingbaijam@kaust.edu.sa
(K.K.S. Thingbaijam), martin.mai@kaust.edu.sa (P.M. Mai).
  [1] Present address: Saint Venant Hydraulics Lab, Université Paris-Est, Chatou, France.
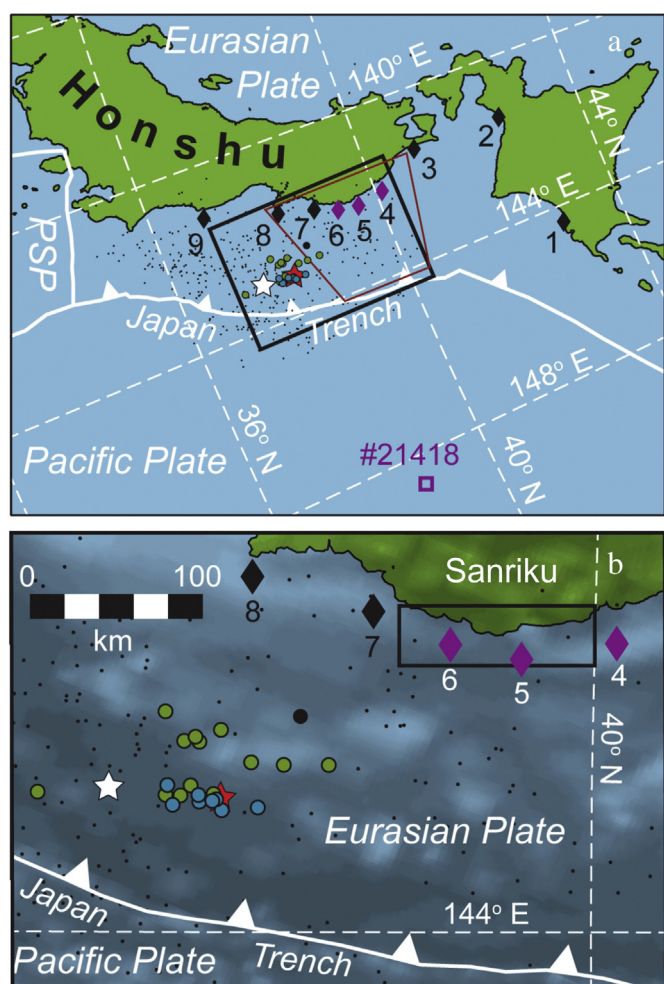
Fig. 1. (a) Seismotectonic setting of the March 11, 2011 Tohoku earthquake. Small black dots are aftershocks (3/11–5/6), which approximate the surface projection of the main rupture. Green and blue circles are locations of centroids for solutions uploaded to the SRCMOD database derived from seismic inversions and tsunami inversions, respectively, and the black dot is the USGS centroid (Table 1). White star is the GCMT centroid, and red star is the average of the centroids obtained by the tsunami waveform inversions. Purple square is DART Buoy 21418, and purple diamonds labeled 4, 5, and 6, respectively, are North Iwate, Central Iwate, and South Iwate GPS buoys, respectively (Locations in Table 2). Other offshore GPS buoys are shown as black diamonds. The brown polygon approximates the footprint of Fig. 4. The black rectangle shows the region shown in panel b. (b) Enlarged view of the rectangle in panel a. Black rectangle is location of Fig. 13a. (For interpretation of the references to color in this figure legend, the reader is referred to the web version of this article.)

damaging event in a nation with extensive networks of seismological, GPS, tsunami, and other geophysical observatories, many inversions of these data to infer its source mechanism have been conducted.

Inversion studies generally divide an assumed earthquake fault plane into numerous subfaults. The Green's functions for unit slip with delta-function time-dependence on each subfault of the rupture plane is computed and, subject to regularization, the linear combination of the Green's functions, weighted by fault displacement (slip vector) for each subfault, that gives the best overall fit to the observed data is determined, usually, but not always, as a function of time. Most inversions analyze only seismic and/or geodetic data of large shallow subduction zone events, but tsunami waveform data, usually in conjunction with geodetic data, are also used in studies which we refer to as "tsunami inversions" (Satake and Kanamori, 1991). The Green's functions for the tsunami waveforms are calculated using an elastic model to determine the seafloor deformation for each subfault and then a long-wave model is used for the propagation of the tsunami waves.

Many studies (primarily inversions, but also some forward modeling studies) of the source mechanism of the Tohoku earthquake analyzed tsunami waveform data recorded at nearshore and offshore buoys together with other data (e.g., Fujii et al., 2011; Gusman et al., 2012; Iinuma et al., 2012; Løvholt et al., 2012; Romano et al., 2012; Grilli et al., 2013; Satake et al., 2013; Yamazaki et al., 2013); however, they all have encountered two problems. First, they had difficulties in reproducing the concentration of elevated wave activity recorded along the Sanriku coast (notably between 39° 30′ and 40° 15′ N); second, even when inverting tsunami waveforms and using dispersive wave Green's functions, they could not satisfactorily reproduce the timing and high-frequency content of tsunami waveforms recorded at the nearshore GPS buoys located in this area, as well as the timing and dispersive wave train at the "Deep-Ocean Assessment and Reporting of Tsunamis" (DART) buoy #21418 located 600 km off the coast (buoy locations in Fig. 1 and waveforms in Fig. 2).

MacInnes et al. (2013, see their Fig. 2) compared simulations of the Tohoku tsunami for ten earthquake source models obtained by inversions utilizing seismic and geodetic data and tsunami waveforms. They found that no model satisfactorily reproduced the amplitude of the runup north of 39° 00′ N (see their Fig. 4). Grilli et al. (2013) inverted geodetic data based on a detailed multi-material finite element model (FEM) of the Japan Trench and forearc and obtained a source model which they called the "UA source" (see Section 7). They then performed forward tsunami simulations, using the UA source and a three-dimensional non-hydrostatic model forced by the time-dependent seafloor deformation. Their simulation reproduced well the long-wave tsunami observed at most nearshore GPS buoys and at DART buoy #21418 as well as the runup and inundation outside of the central Sanriku area. However, they could not reproduce the elevated tsunami runups and inundation measured along the central Sanriku coast between 39° 30′ and 40° 15′ N, nor the large amplitude higher-frequency waves at the three Iwate GPS buoys located off Sanriku (Fig. 2d–f; labeled 4, 5, and 6 in Fig. 1b) and the dispersive wave train at DART buoy #21418 (Fig. 2j). At all four of the above buoys the residuals (the difference between the observed and simulated waves) for the UA source (Fig. 2d–f; j) clearly suggest a second wave train, 3–5 m in height with a dominant period of 3–4 min, much shorter than that of the waves earlier in the record, arriving between 25 and 32 min after the earthquake. At DART buoy #21418 (Fig. 2j), the 2 m elevation leading crest can be fully explained by the UA seismic source but the following residual wave train, composed of at least six cycles of 3 to 4 min period waves up to 1.7 m in height, cannot. Grilli et al. (2013) concluded that the residual waves at the buoys could not be explained only by the displacement of the seafloor caused directly by the slip on the fault (which we call an "earthquake-only" source) and that an additional, secondary, tsunami source was also required.

The two most likely mechanisms for a secondary tsunami source are out-of-sequence (splay) faulting or a submarine mass failure (SMF). Of these, there is no evidence for out-of-sequence splay faulting in the published seismic profiling data for the source region (e.g. Tsuru et al., 2002); in addition, any splay faulting would have generated seismic waves that would have been detected by the dense network of GPS receivers or seismometers in Japan, unless it was very localized (MacInnes et al., 2013). There is, however, considerable evidence supporting the possibility of an SMF. Large slumps are found on the margin of the accretionary prism off the Sanriku coast (Cadet et al., 1987; von Huene et al., 1994; Tsuru et al., 2002) and data from two ocean bottom pressure gauge stations TM1 and TM2 off Kamaishi (latitude 39°12′ N) indicate that at least part of the tsunami source in this region is a narrow area in the deeper part of the Japan Trench (Maeda et al., 2011). The short-period waves recorded at nearshore buoys and the offshore DART buoy #21418 nearest Japan (i.e., the residual waves shown in Fig. 2) are indicative of an SMF (e.g., Grilli and Watts, 2005; Tappin et al., 2008) and, as shown by Grilli et al.'s (2013) forward simulations, cannot be reproduced by an earthquake-only source. The peaked and focused
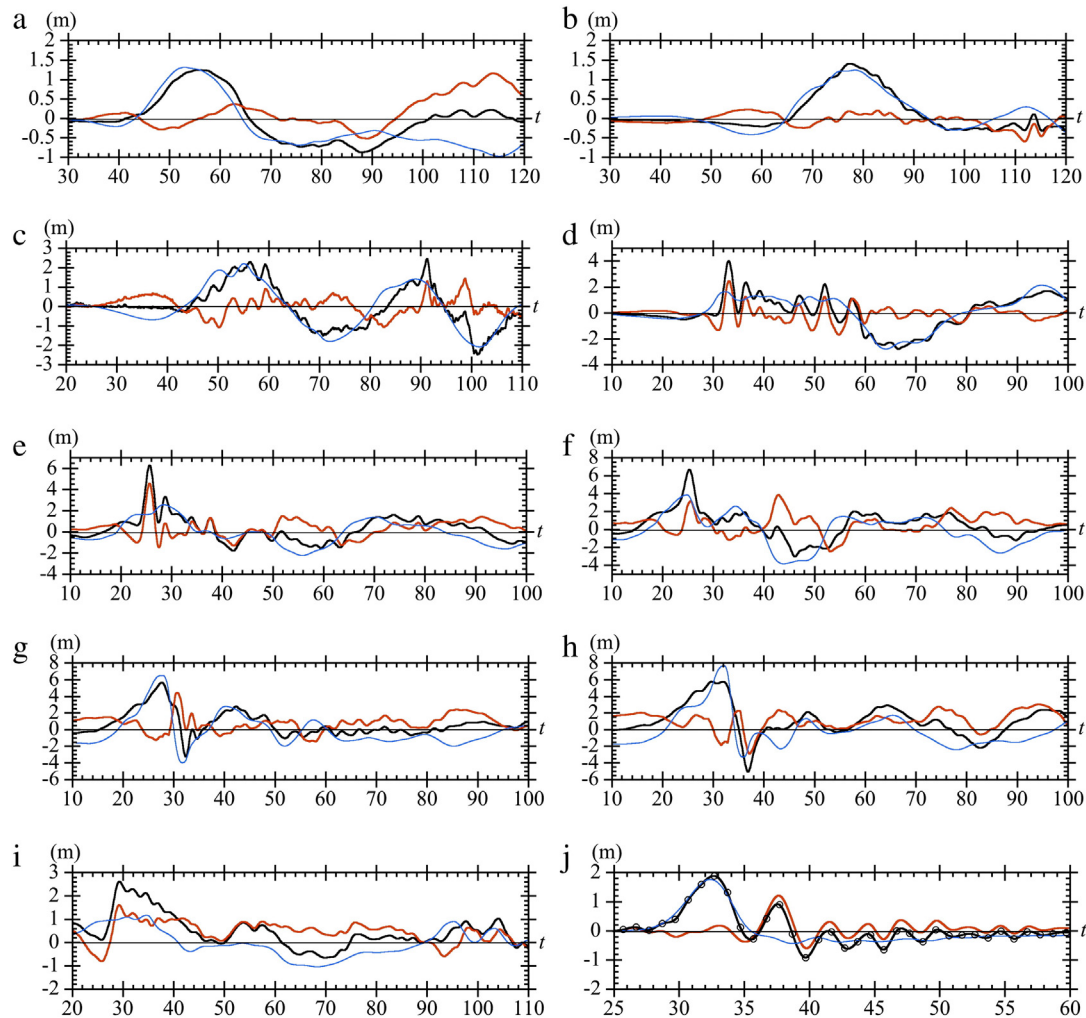
Fig. 2. Tsunami waveforms (surface elevations) at buoys near Japan as a function of time. Panels (a) to (i) are 1st–9th GPS stations offshore the coast (for location see Figs. 1, 8 and 11 and Table 2): (a) Kushiro; (b) Tomakomai; (c) Matsu Ogawara; (d) North Iwate; (e) Central Iwate; (f) South Iwate; (g) North Miyagi; (h) Central Miyagi; (i) South Miyagi; (j) DART buoy #21418 (the black circles show actual data points which have been interpolated by a spline curve). Observed data at GPS buoys and the DART buoy (black) are compared to synthetics for the UA earthquake source (light blue). The red trace is the residual (the difference between the observed data and synthetic). (For interpretation of the references to color in this figure legend, the reader is referred to the web version of this article.)

flow depths and runup elevations along the northernmost Sanriku coast are also characteristic of an SMF-generated tsunami because they are more directionally focused than would be expected for an earthquake-only source (Grilli et al., 2002; Enet and Grilli, 2007; Tappin et al., 2008).

A second tsunami source off Sanriku was also suggested by Fujii et al. (2011, p. 819), on the basis of their tsunami inversion, and Satake et al. (2013) noted an ~100 km latitude offset between the locations of the largest fault slip and the maximum coastal tsunami height. Ichihara et al. (2013) reported an electromagnetic signal that they interpreted as evidence for a secondary tsunami source near the trench axis located well to the north of the GCMT centroid, initiating about 1 min after the earthquake's origin time.

Regarding the likelihood of earthquake-triggered SMFs, marine surveys at the latitude of the earthquake epicenter (~38° N) reveal recent seabed movement (Fujiwara et al., 2011); and Kawamura et al. (2012, 2014) proposed that this is evidence for a major landslide triggered by the Tohoku earthquake (area approximately delimited by the dashed white curve in Fig. 3 and white ellipse in Fig. 4) that could be an additional tsunami source. The region off Sanriku is where the catastrophic Great Meiji tsunami of 1896 was generated, the source mechanism of which has been a matter of considerable speculation. The relatively small magnitude of the 1896 earthquake suggests that the tsunami was generated either by a 'slow' event (Kanamori, 1972) or by rapid up-lift of the sediment wedge (Tanioka and Seno, 2001); alternatively it

could have been due to a submarine landslide (Kanamori and Kikuchi, 1993).

The primary objective of this study, therefore, is to determine whether a tsunami generated by a "dual source," i.e., the combination of an earthquake and an SMF, can explain the on- and offshore tsunami data for the 2011 Tohoku event. To do this we proceed as follows. We first show there is a discrepancy between the centroid obtained by source inversions using tsunami data and that obtained using only long-period seismic waves. We next identify the most likely SMF source location from backward ray tracing of high-frequency tsunami waves observed at buoys off Sanriku. We locate and parameterize the most likely SMF using marine geophysical data, and then validate and test the proposed SMF mechanism by a simplified slope stability analysis. We simulate the tsunami waveforms using a dual source (an earthquake combined with the proposed SMF). We use a three-dimensional (3D) non-hydrostatic model, forced by the time-dependent sea bottom motion from the dual source. Tsunami propagation is modeled using a fully non-linear and dispersive long-wave Boussinesq model. Computations are performed in a series of nested grids with increasingly fine resolution to-wards the shore. We validate our results by comparing simulations to measured onland runup and inundation data and also to tsunami wave-forms recorded at nearshore buoys and the DART buoy, on which, in ad-dition, we perform a time-frequency wavelet analysis. Finally, we compare the observed data to the synthetic tsunami waveforms from
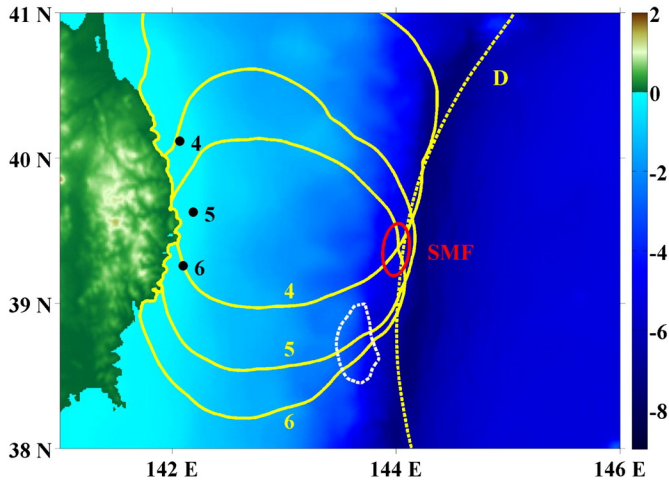
Fig. 3. Travel paths (solid and dashed yellow lines) computed taking bathymetry into account, based on linear (dispersive) wave phase velocity (GPS #4–6) or group velocity (DART #21418; D), for the higher-frequency leading elevation wave, with period $T =$ 4 min, observed at the buoys (time series shown in Fig. 2d–f,j–black line). The proposed SMF tsunami source is outlined in red; the region of slumping observed in earlier field surveys (Kawamura et al., 2012) is outlined in white (dashed). Computed travel times are: (GPS #4) North Iwate: 33.1 min; (GPS #5) Central Iwate: 25.7 min; (GPS #6) South Iwate: 25.3 min; DART #21418: 37.6 min. Note that a 198 s triggering delay was assumed from the start of the earthquake (equal to the end of the SMF motion–see Section 7). Color scale is bathymetry/topography in km from ETOPO-1 data. (For interpretation of the references to color in this figure legend, the reader is referred to the web version of this article.)

our dual source model and to waveforms from other studies for which we had data.

2. Inversions for earthquake source parameters

Many "seismic inversions" (i.e., inversions whose dataset does not include any tsunami waveform data) have inferred source models for the Tohoku earthquake. Of these, the mechanism (centroid and moment tensor) obtained by the Global CMT Project, (abbreviated as GCMT below; Nettles et al., 2011) may be regarded as the best overall representation of the earthquake source, because it is based on long-
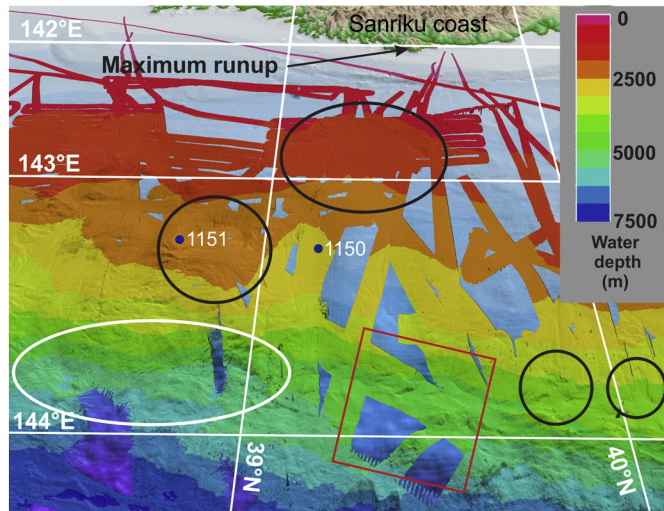

Fig. 4. Submarine mass failures (SMFs) in the region off northern Tohoku (Sanriku) coast from pre-March 2011 JAMSTEC bathymetry. Black ellipses: SMFs. Red square: the location of the SMF triggered by the March 2011 earthquake (see Fig. 5). White ellipse is the location of the submarine landslide identified by Kawamura et al., 2012. The blue dots are the locations of the sites drilled during ODP leg 186. Highest elevation observed tsunami runup/inundation (around 39.5° N) along the Sanriku coast is also marked. Approximate location of this figure shown by brown polygon in Fig. 1a. (For interpretation of the references to color in this figure legend, the reader is referred to the web version of this article.)

period (300–500 s) seismic wave data from observatories throughout the world, and was obtained following procedures that have been honed over several decades. If the source models obtained by tsunami inversions accurately represented the overall source of the Tohoku earthquake, their slip centroids should agree with the centroid obtained by the GCMT inversion. We now examine whether or not this is the case.

21 source models for the Tohoku 2011 earthquake have been uploaded by various researchers to the SRCMOD database (http://equake-rc.info/srcmod/). Each model specifies the detailed spatial (and sometimes also temporal) slip history on an assumed fault plane(s) obtained by a particular study. Multiple models have been uploaded by some authors, including results for some models categorized as preliminary. With the exception of the GCMT and U.S. Geological Survey (USGS) solutions, we do not consider source models which are not available through the SRCMOD database. Table 1 shows the computed latitude, longitude and depth of the centroids of the final slip distribution for each of these 21 models, as well as the GCMT centroid (white star) and the centroid of the USGS solution. A "T" in the "Type" column of Table 1 identifies a tsunami inversion. The centroids are shown in Fig. 1, and the average centroid for the eight tsunami inversions is also shown in Table 1 and Fig. 1 (red star; see caption for Fig. 1 for other details). It is notable that the centroids obtained by the various solutions are widely scattered. This has not been previously recognized (although Løvholt et al., 2012, noted the scatter of other source parameters obtained by various studies), and suggests that further work on seismic source inversion methods is needed.

The tsunami inversion centroids shown in Table 1 and Fig. 1 are clustered within a 30 km radius of their average centroid (the red star in Fig. 1). On the other hand, the red star is about 60 km NNE of the

Table 1
Earthquake source solutions.

No	Type[a]	Author	Tag[b]	Lon°	LAT°	Z (km)
1		Ammon et al. (2011)	01AMMO	142.51	37.82	19.93
2	T	Fujii et al. (2011)	01FUJI	142.90	38.03	18.58
3	T	Gusman et al. (2012)	01GUSM	143.01	37.91	17.04
4		Hayes (2011)	01HAYE	142.65	37.98	24.39
5		Ide et al. (2011)	01IDEx	142.67	38.09	30.22
6		Lay et al. (2011)	01LAYx	143.03	37.18	14.57
7	T	Satake et al. (2013)	01SATA	142.92	38.10	17.80
8		Shao et al. (2011)	01SHAO	142.69	37.92	16.77
9		Wei and Sladen[c]	01WEIx	142.84	38.45	19.85
10		Yagi and Fukahata (2011)	01YAGI	143.03	37.91	20.88
11	T	Yamazaki et al. (2011)	01YAMA	143.11	38.30	16.11
12		Yue and Lay (2013)	01YUEx	142.94	37.86	24.02
13	T	Fujii et al. (2011)	02FUJI	142.88	38.10	19.00
14	T	Gusman et al. (2012)	02GUSM	142.99	38.05	17.18
15	T	Satake et al. (2013)	02SATA	142.93	38.11	13.88
16		Shao et al. (2011)	02SHAO	142.68	37.99	16.52
17		Wei et al.[d]	02WEIx	142.83	38.68	19.22
18	T	Satake et al. (2013)	03SATA	143.07	38.13	10.93
19		Shao et al. (2011)	03SHAO	142.97	37.96	20.28
20		Wei et al. (2012)	03WEIx	142.82	38.28	16.65
21		Shao et al. (2011)	04SHAO	143.04	37.84	19.04
22		USGS[e]	–	142.60	38.49	10.00
23		GCMT[f]	–	143.05	37.52	20.00
		Tsunami average		142.98	38.09	16.32

[a] T indicates tsunami inversion.

[b] The Tag column gives the ID in the SRCMOD project database. All entries start with s2011TOHOKU.

[c] Wei, S., Sladen, A., 2011. Preliminary Result 3/11/2011 (Mw 9.0), Tohoku-oki, Japan. http://www.tectonics.caltech.edu/slip_history/2011_tohoku-oki-tele/index.html (last accessed July 1, 2013).

[d] Wei S., Sladen, A., and the ARIA group, 2011. Updated Result 3/11/2011 (Mw 9.0), Tohoku-oki, Japan. http://www.tectonics.caltech.edu/slip_history/2011_taiheiyo-oki/index.html (last accessed July 1, 2013).

[e] http://earthquake.usgs.gov/earthquakes/eqinthenews/2011/usc0001xgp/neic_c0001xgp_cmt.php.

[f] http://earthquake.usgs.gov/earthquakes/eqinthenews/2011/usc0001xgp/neic_c0001xgp_gcmt.php.

GCMT centroid (the white star in Fig. 1). This discrepancy between the GCMT centroid and the average centroid of the tsunami inversions appears to be significant, although the heterogeneous nature of the data precludes a formal statistical error analysis.

The tsunami inversions explain the tsunami waveform data (e.g., Fig. 2) solely as a direct consequence of displacement of the sea floor caused by slip on the fault; this could lead to centroids which are systematically biased to the north if part of the tsunami on the Sanriku coast (which is well to the north of all of the centroids) was generated by a secondary source which was not included in the model parameterizations used by the tsunami inversions. It is notable that the source models obtained by the tsunami inversions all require fault slip along a narrow strip near the trench axis extending north to the Sanriku region, whereas seismic inversions do not infer significant fault slip there (see Fig. 4 of Koketsu et al., 2011).

3. Initial modeling and identification of a possible SMF location

Omitting details, we found that modeling of the SMF sources identified by Fujiwara et al. (2011) and Kawamura et al. (2012) (white curves in Figs. 3 and 4) failed to generate sufficiently large high-frequency waves and also failed to match the observed relative arrival times at the three Iwate nearshore buoys and the DART buoy; furthermore, the tsunami resulting from the earthquake and these SMFs did not reproduce the elevated 30–40 m runups along the Sanriku coast. This suggested that the large amplitudes of the higher-frequency residual waves measured at the GPS buoys required a much larger volume SMF source which is located further to the north.

A backwards travel time analysis (Fig. 3) was applied to tentatively locate the SMF, based on wave-ray theory and solving the eikonal equation (which governs linear wave geometric optic theory) using a fast-marching algorithm. Assuming that waves generated by the SMF can be modeled by linear wave theory, we have in water depth h the phase velocity (Dean and Dalrymple, 1984),

$$c_p = \frac{L}{T} = \frac{\omega}{k} = \sqrt{\frac{g}{k}\tanh kh}, \tag{1}$$

where ω is the wave angular frequency, k the wavenumber, $L = 2\pi/k$ the wavelength, and $T = 2\pi/\omega$ the period, and the group velocity is,

$$c_g = \frac{1}{2}c_p\left(1 + \frac{2kh}{\sinh 2kh}\right). \tag{2}$$

Eqs. (1) and (2) include frequency dispersion, which is important for accurately estimating the travel time of the observed 3–4 min period waves. If the waves were modeled as traveling at their long-period wave speed (e.g., such as by Ito et al., 2011), their velocity would be overestimated, and the location of the SMF tsunami source would be misplaced too far south (see below).

Fig. 3 shows the wave-ray travel paths computed as a function of bathymetry, based on $c_p(h)$ or $c_g(h)$, for the three Iwate GPS buoys and the DART #21418 buoy, respectively, for the first leading elevation residual wave, with an assumed period $T = 4$ min. The analysis identifies the inferred area of origin (red ellipse in Fig. 3) of the waves attributed to a secondary tsunami source, between 39° 6′ and 39° 42′ N (along a longitude of about 144° E), but most probably around 39° 24′ N. The computed travel times are: (#4) North Iwate: 33.1 min; (#5) Central Iwate: 25.7 min; (#6) South Iwate: 25.3 min; DART #21418: 37.6 min. To accurately reproduce the arrival times at both the GPS and the DART buoys, we found that a triggering delay of about 198 s after the initiation of earthquake rupture was required. This time includes both the delay corresponding to initiation of SMF motion by seismic waves traveling from the main rupture area and the duration of SMF motion, when the tsunami waves, whose travel path we compute, have been fully generated.

The detailed modeling of the SMF tsunami generation presented below confirms the above estimate of the SMF location. Despite the significant amplitude of the residual waves (several meters at the buoys) and their smaller wavelength than the earthquake-generated waves, they remain of small steepness. Hence their phase velocity is well represented by the linear dispersion relationship (Eq. (1)). As discussed above, including the effect of dispersion is key to the accuracy of this analysis. Hayashi et al. (2011) used linear shallow water wave (LSWW) theory to perform a similar ray tracing analysis on the primary wave crests recorded at underwater pressure gauges (Maeda et al., 2011; Ito et al., 2011) and GPS buoys. Neglecting dispersion led to overestimating wave speed and resulted in the origin of the higher-frequency tsunami waves being sited too far to the south. Indeed, at the three Iwate GPS buoys, the primary crests of the 3–4 minute period waves have a threshold depth h_{SW} for LSWW theory to apply that satisfies $kh < \pi/10$, yielding (Dean and Dalrymple, 1984),

$$c_{pSW} = \frac{L}{T} = \frac{\omega}{k} = \sqrt{gh} = c_{gSW}$$

$$\text{for } h < h_{SW} = \frac{gT^2}{400} \text{ and } \frac{c_p}{c_{pSW}} = \sqrt{\frac{\tanh kh}{kh}} \leq 1 \tag{3}$$

where SW refers to the non-dispersive LSWW approximation. For a $T = 180$ s period wave, we find $h_{SW} = 795$ m. Hence, Hayashi et al.'s analysis is flawed because, for $h \gg h_{SW}$ (which is true for most of the propagation; see Fig. 3), the dispersive Eqs. (1) and (2) must be used, yielding $c_p < c_{pSW}$.

4. Evidence for an SMF at the proposed location

We looked for an SMF with evidence of recent seabed movement in the area of the secondary tsunami source tentatively identified by the backward ray tracing (Fig. 3). On post-earthquake Multi-Beam Echo Sounder (MBES) surveys conducted by the Japan Agency for Marine-Earth Science and Technology (JAMSTEC, 2011), we located a number of large-volume slumps (Fig. 4) one of which, at a depth of about 4000–5500 m (Fig. 5), correlates with the identified area. This SMF is $w = 40$ km wide, with a downslope length from the headwall
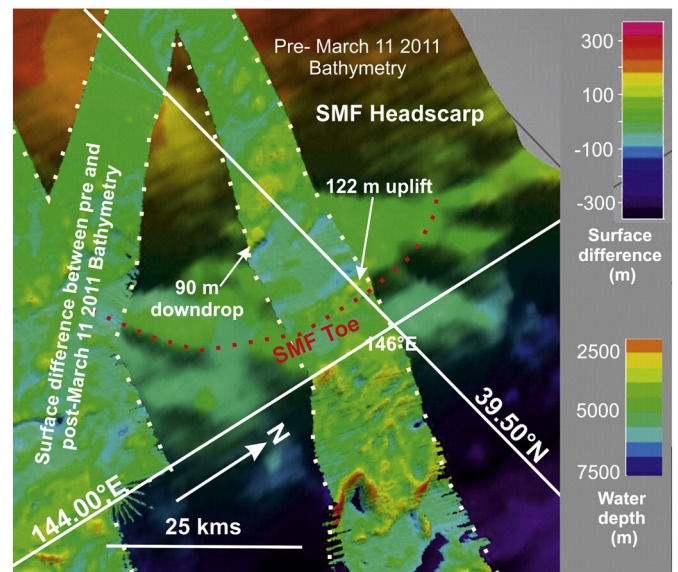

Fig. 5. Difference in seabed elevation between pre- and post-March 11, 2011 MBES bathymetry. Post-March 11th MBES are the swaths between white dotted lines, with pre-March 11 bathymetry shown elsewhere. The pre-March 11th bathymetry is from the Japan Oceanographic Data Center and gridded at 500 m. The post-March 11th data is 12 kHz MBES gridded at 100 m. Note SMF headscarp, downdrop at rear of SMF and uplift at SMF toe. See Fig. 4 for location. (For interpretation of the references to color in this figure legend, the reader is referred to the web version of this article.)

$b = 20$ km. Comparison of the post-earthquake MBES data with pre-earthquake data from the Japan Oceanographic Data Center (JODC) suggests that the SMF was a short-amplitude rigid slump that was triggered by the March 11 earthquake (Fig. 5). There were significant seabed elevation changes, well in excess of the relative error expected for data sets with different resolutions acquired at different times. The inferred seabed morphology change is consistent with a short-amplitude, rotational mechanism, which is characteristic of slump failure. This interpretation also is consistent with Multichannel Seismic (MCS) data in this area, on which slumps are present (Tsuru et al., 2002). The maximum uplift on the trenchward side of the SMF is about 100 m, with a maximum downdrop at the landward side of about 90 m; values consistent with rotational slumping movement. For slumps, maximum thickness Th is about 10% of the slump length b (Watts et al., 2005 and references therein), which yields a maximum thickness Th of about ~2000 m. This thickness is near the upper bound for pre-earthquake slumps identified in the area (von Huene et al., 1994; Tsuru et al., 2002) and gives an SMF volume in the order of $V \sim 500$ km^3 (assuming a quasi-Gaussian shape with elliptical horizontal footprint; Enet and Grilli, 2007; see details below).

5. Slope stability analysis

To support our hypothesis that the SMF identified as the secondary tsunami source could have failed as a result of horizontal seismic acceleration from the March 11 earthquake, we performed a simplified (first-order) geotechnical slope stability analysis using the Bishop method (Bishop, 1955; Turner and Schuster, 1996). To the north and south of the location of the secondary SMF source estimated by the travel time analyses (Fig. 3), using pre-earthquake seabed morphology, we selected 5 parallel and equidistant transects spaced at 0.4° in latitude and oriented in direction $\theta = 97°$ from North (Fig. 6). The transects are 140 km long and roughly perpendicular to the Japan Trench axis (1–5 in Fig. 6 and Table 3); transects #3 and #4 lie either side of our candidate SMF (around 39° 30′ N, 144° E Fig. 3). These transects appear realistic because ~30 km long, 2–3 km thick SMFs are shown in the area of transects #1–3 in Tsuru et al. (2002, Fig. 6). The region of high seabed slope along transect #5 (around 38° 50′ N, 144° 40′ E) is where Kawamura et al. (2012) found evidence of recent slumping (Figs. 3 and 4). Fujiwara et al. (2011) reported landslide debris, 1–2 km across, farther south at around 38° N.
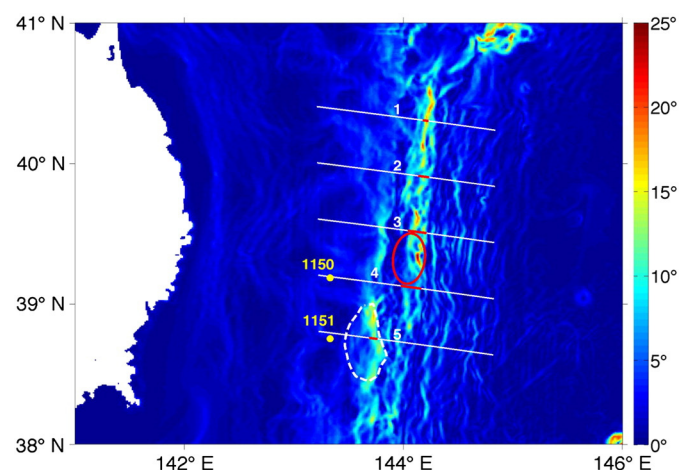

Fig. 6. Pre-earthquake average seafloor slope (degrees) in the SMF source area (for detail see Fig. 4), with white lines marking the direction (azimuth θ) and extent of transects analyzed with the 2D slope stability model Slide (Fig. 7, Table 3). Red segments indicate the extent of failure surfaces predicted along each transect. The white dashed region shows the extent of the slumping observed by Kawamura et al. (2012), and the red ellipse shows the SMF location simulated in NHWAVE. Bathymetry used in the figure is 1′ arc ETOPO1 data. The yellow dots show the locations of ODP sites 1150 and 1151. (For interpretation of the references to color in this figure legend, the reader is referred to the web version of this article.)

Table 2
Locations and water depths of the GPS buoys and DART #21418.

Buoy No/letter	Name	Water depth (m)	Latitude	Longitude
1 or a	Kushiro	50.1	42° 54′ 38″ N	144° 23′ 50″ E
2 or b	Tomakomai	50.7	42° 32′ 39″ N	141° 26′ 46″ E
3 or c	Matsu Ogawara	43.8	40° 55′ 30″ N	141° 25′ 27″ E
4 or d	North Iwate	125	40° 07′ 00″ N	142° 04′ 00″ E
5 or e	Central Iwate	200	39° 37′ 38″ N	142° 11′ 12″ E
6 or f	South Iwate	204	39° 15′ 31″ N	142° 05′ 49″ E
7 or g	North Miyagi	160	38° 51′ 28″ N	141° 53′ 40″ E
8 or h	Central Miyagi	144	38° 13′ 57″ N	141° 41′ 01″ E
9 or i	South Miyagi	137	36° 58′ 17″ N	141° 11′ 08″ E
DART #21418	DART #21418	5700	38° 41′ 7″ N	148° 46′ 09″ E

As we lack site-specific geotechnical data, sediment properties were taken from the Ocean Drilling Project (ODP) Leg 186 sites 1150 and 1151 (Fig. 6) (Suyehiro et al., 2003). The sites are located 60 km to the west of the slumps we locate on our MBES on the margin of the accretionary prism (Fig. 4). The sediment at the ODP sites is dominantly diatomaceous silty clay and claystone with a typical bulk density of 1.5 g/cm^3 (unit weight of 14.7 kN/m^3) and cohesion of 60 kPa; no pore pressure data were available. Triggering of the SMFs was assumed to be through a combination of earthquake-generated, horizontal seismic acceleration (shear waves) and excess pore pressure build-up, which are mechanisms recognized as significant in driving SMF along convergent margins by inducing a rapid loss of frictional strength along a failure surface (Tappin et al., 2008). The Bishop method quantifies the potential for failure of a given slope by computing a balance of seismic and gravitational forces, together with frictional stability, for a series of selected potential failure surfaces. For each slope, a Factor of Safety (FS), defined as the ratio of disturbing (i.e., seismic, gravity, and pore pressure) to stabilizing (i.e., shear and cohesiveness) forces, is computed to select the likeliest slip surface and SMF geometry for a minimum FS value. In the absence of pore pressure data, we performed an idealized pseudo-static two-dimensional (2D) analysis, with an assumed horizontal seismic load as a trigger. Because the SMF is within the compressional quadrant of the earthquake (see Fig. 7 in Grilli et al., 2013), we assumed that positive, earthquake induced, pore pressures decreased the effective stress on the frictional surfaces, thus increasing the potential instability.

Because of the lack of data and the many simplifications, the following stability analysis only provides relative results, i.e., it will just identify which of the transects is likeliest to fail. Should site-specific field data become available in the future, a more detailed and thorough slope stability analysis can be performed. Along each transect, RocScience's model Slide (http://www.rocscience.com/products/8/Slide) was used to compute slope stability for vertical 2D sections, with the domain extending 10 km below sea level. An internal friction angle of 35° is assumed. Simulated annealing is applied in Slide to find an arbitrary (non-circular) failure surface for each transect. In this automatic mode, Slide computes FS for a large number of failure surfaces and retains the minimum value. If the minimum FS value for a given 2D

Table 3
Slide 2D stability analyses. Location and geometrical description of five transects #1–5 (Fig. 6) oriented in direction $\theta = 97°$ from North (Fig. 9); x_f and y_f mark the center of the failed surfaces; l and T are SMF length and maximum thickness computed from the 2D stability analysis; factor of safety FS was computed for a seismic loading coefficient $k_s = 0.3$.

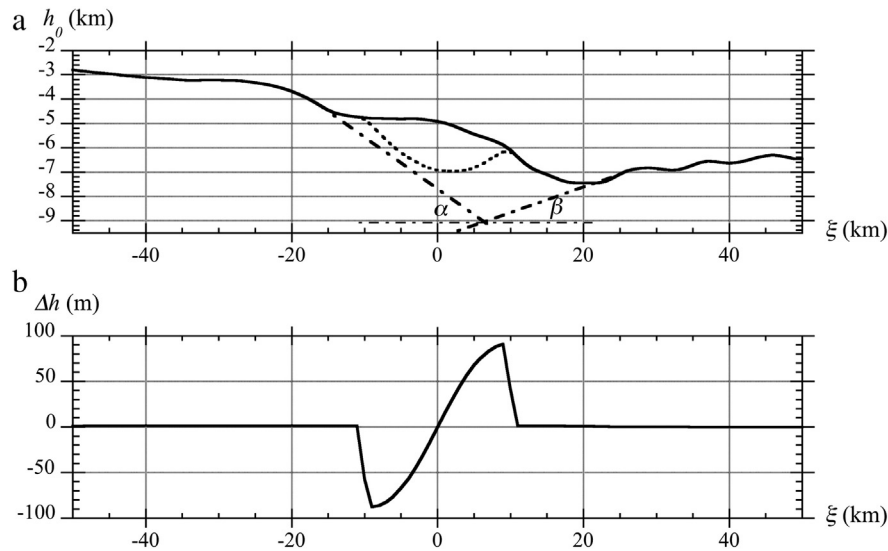| Transect	x_f (lon)	y_f (lat)	l (km)	T (m)	FS ($ks = 0.3$)
#1	144.20	40.30	4.25	320	0.549
#2	144.18	39.90	8.48	477	0.610
#3	144.13	39.51	14.57	569	0.595
#4	144.07	39.12	16.29	644	0.670
#5	143.73	38.75	6.95	419	0.619

Fig. 7. Vertical cross-section through the center of modeled SMF (red ellipse with center of mass at 39.37° N, 144.00° E in Figs. 3 and 6) in azimuthal direction $\theta = 97°$ from North (see Fig. 9). (a) Seafloor bathymetry (upper solid line); assumed SMF failure surface in tsunami simulations (dashed line; for SMF geometry of Eq. (5)); normal fault with headwall angle $\alpha = 12°$ and subducting Pacific plate with dip angle $\beta = 6°$ (chained lines). (b) Vertical seafloor deformation caused by SMF $\Delta h = h - h_0$ (see Eq. (7)). Distance is measured from the SMF center of mass.

transect is less than 1, there is failure along the corresponding slip surface. Without seismic loading, all transects were found to be stable ($FS > 1$). Imposing a seismic loading coefficient of $k_s = 0.3$, corresponding roughly to a peak horizontal acceleration of 0.3 g, a reasonable assumption for the region during the Tohoku event, *Slide* predicted that all 5 transects fail with a $FS < 1$ (Table 3). However, the only failures large enough to generate a significant tsunami, of length, $l = 15$–16 km, are along transects #3 and #4 (Fig. 6). The largest failure, with nearly the lowest FS value, is between these transects, with a center of motion at 39° 22′ 12″ N, 144° E, a location that correlates with the SMF identified from the travel time analysis (Fig. 3) and is clearly visible on the MBES data (Figs. 4 and 5). The SMF on the MBES is larger, but consistent in length with the prediction from *Slide*. The FS values (Table 3) are also low for the other transects, suggesting that, along these, there would also be SMFs, but that they would be shorter in length and thus much smaller in volume. If triggered, these SMFs would contribute little to tsunami generation for the 2011 event; however, on the MBES we could not identify any other significant failures along the other transects, except for the failure along transect #5 (Kawamura et al., 2012). As noted above, however, our initial modeling showed this not to be of sufficient volume to generate a significant tsunami. In summary, the stability analysis, although simplified and "first-order," suggests that our proposed SMF was the most likely to fail of all those in the region off Sanriku under the loading of the 2011 earthquake.

6. Wave propagation modeling-methodology for tsunami simulation

As most large earthquakes generate long-wavelength tsunamis, it has been widely assumed that dispersive effects are small and, because of this, they can be accurately simulated using non-dispersive nonlinear shallow water (NSW) wave equation models such as BMs (e.g., Kowalik and Murty, 1993; Satake, 1995). More recently, however, it has been recognized that when the distances traveled are long this assumption may be incorrect (Glimsdal et al., 2013), and that, in the far-field, earthquake-generated tsunamis may become more dispersive than previously believed. Thus, dispersive long-wave models have been increasingly used to simulate earthquake tsunamis such as for example, the 2004 Indian Ocean event (Horrillo et al., 2006; Grilli et al., 2007; Ioualalen et al., 2007) and others (e.g., Grilli et al., 2010), including

Tohoku 2011 (Løvholt et al., 2012; Grilli et al., 2013; Kirby et al., 2013). For short propagation distances, however, dispersive effects should be small for earthquake-generated tsunamis, as confirmed by Grilli et al.'s (2013) near-field simulations of the Tohoku 2011 tsunami based only on the UA earthquake source. In contrast, in the far-field, Kirby et al. (2013) found that dispersive effects reached $\pm 60\%$ of the surface elevation.

Due to their smaller source area, SMF-generated tsunamis have shorter wavelengths and thus are more dispersive, even in the near-field. Hence, they are best simulated using dispersive long-wave BMs (e.g., Wei et al., 1995; Watts et al., 2003; Lynett and Liu, 2005; Løvholt et al., 2008; Tappin et al., 2008; Fuhrman and Madsen, 2009; Shi et al., 2012) or other types of models which are both nonlinear and fully dispersive (e.g., Grilli and Watts, 1999, 2005; Grilli et al., 2002; Abadie et al., 2010; Ma et al., 2012, 2013). For the 2011 Tohoku event, as noted above, short-period, dispersive waves characterize the tsunami waveform buoy data (e.g., Fig. 2d–f, j); therefore to fully simulate them, a dispersive long-wave model, such as a BM, is required, particularly when considering an additional SMF source.

To accurately model the earthquake-generated tsunami the time-history of the displacement of the sea floor must be appropriately accounted for by a space- and time-varying boundary condition, rather than simply imposing a "hot start" (e.g., Grilli et al., 2013; Yamazaki et al., 2013). This is especially true for an extremely large event like the 2011 Tohoku for which seismic inversions (e.g., Ide et al., 2011; Yue and Lay, 2011) show that the main earthquake rupture lasted 3–4 min. This type of modeling, in which seafloor deformation is triggered as a time sequence, had already been found necessary for accurately simulating tsunami generation for the 2004 Indian Ocean tsunami, which was also generated by an extremely large earthquake with a very long duration (Grilli et al., 2007; Ioualalen et al., 2007).

We model the Tohoku tsunami generation for the dual source using the 3D non-hydrostatic model NHWAVE (Ma et al., 2012), in which seafloor deformation from the earthquake (UA source) and the SMF is specified as a time- and space-dependent bottom boundary condition. NHWAVE solves 3D Euler equations for incompressible flows in a σ (vertical) coordinate framework (i.e., boundary fitted, typically with 3–7 levels), with the simplifying assumption of a single-valued water surface displacement. NHWAVE has been validated (Ma et al., 2012)

for highly dispersive landslide tsunami generation by comparing simulated surface elevations to measurements in laboratory experiments (Enet and Grilli, 2007).

After the initial generation of the waveform in NHWAVE (here at $t = 300$ s), the computed surface elevation and depth-averaged horizontal velocity fields are used to initialize FUNWAVE-TVD (Shi et al., 2012), a fully nonlinear two-dimensional (2D) BM with extended dispersive properties, in which waves are propagated to the coast in a series of increasingly refined nested grids, using a one-way coupling procedure (details are discussed below).

FUNWAVE was initially developed for coastal wave dynamics (Wei et al., 1995; Chen et al., 2000, 2003; Kennedy et al., 2000), and later applied to tsunamis (Watts et al., 2003; Day et al., 2005; Grilli et al., 2007, 2010; Ioualalen et al., 2007; Tappin et al., 2008). FUNWAVE-TVD (Shi et al., 2012; Kirby et al., 2013) is a more recent implementation, using a "Total Variation Diminishing" (TVD) shock-capturing algorithm that more accurately simulates wave breaking dissipation and coastal inundation; once wave breaking is detected (based on a breaking criterion) the model is switched to NSW equations in regions where this occurs. The model was also efficiently parallelized on computer clusters using the Message Passing Interface (MPI) protocol, allowing for the modeling of large grids in a reasonable time. FUNWAVE-TVD was validated against a comprehensive set of analytical, laboratory, and field benchmarks, as part of the development of tsunami hazard maps for the US East Coast (Tehranirad et al., 2011) and was used by Grilli et al. (2013) and Kirby et al. (2013) to simulate the near- and far-field effects of the Tohoku earthquake-only tsunami.

7. Tsunami generation and propagation

Most earthquake rupture models used in tsunami studies assume a superposition of dislocations on faults embedded in either a homogeneous or layered elastic domain, having a free surface boundary condition (e.g., Miyazaki et al., 2011; Ozawa et al., 2011; Shao et al., 2011; Simons et al., 2011). However, neither a homogeneous nor a layered elastic system adequately represents the complex geometry and structure of the Japan wedge and subducting slab. To address this complexity, Grilli et al. (2013) simulated fault-slip driven elastic dislocation deformation of the subduction zone, using the Finite Element Method (FEM) to account for the actual geometry of the Japan Trench and its forearc, as well as the 3D inhomogeneous structure of material properties in the subduction zone (i.e., the stiff subducting Pacific Plate and relatively weak forearc and volcanic arc of the overriding plate). As noted above, we call their solution the "UA source" and the fault slip distribution from this was estimated by analyzing onshore and offshore geodetic data (Sato et al., 2011) using FEM-based inverse methods (Masterlark and Hughes, 2008; Kyriakopoulos et al., 2013).

NHWAVE simulations of the dual source are performed up to $t = 300$ s in a 3D grid with a 1000×1000 m horizontal resolution and five σ layers in the vertical direction (Fig. 8). The earthquake component of the tsunami is based on the UA source, with the timing of the earthquake rupture obtained from Yue and Lay (2011). The space- and time-dependent triggering of the seafloor deformation from earthquake faulting is initiated at time $t = 0$. The SMF motion, detailed below, is triggered at time t_i. The output (surface elevation and horizontal velocity components at the required depth) is then used to initialize FUNWAVE-TVD over the same resolution grid. Computations are then conducted by a one-way coupling procedure in nested 250 m and 50 m grids (Fig. 8), as also used by Grilli et al. (2013): time series of free surface elevation and currents are computed in a coarser grid, for many "numerical gauges" along the boundary of the next finer grid level; computations are then restarted in the finer nested grid, using the time series as boundary conditions. To represent open boundary conditions, sponge (absorbing) layers are specified along the offshore boundary of the coarser 1000 m resolution FUNWAVE-TVD grid. Because time series computed at "numerical gauges" along the
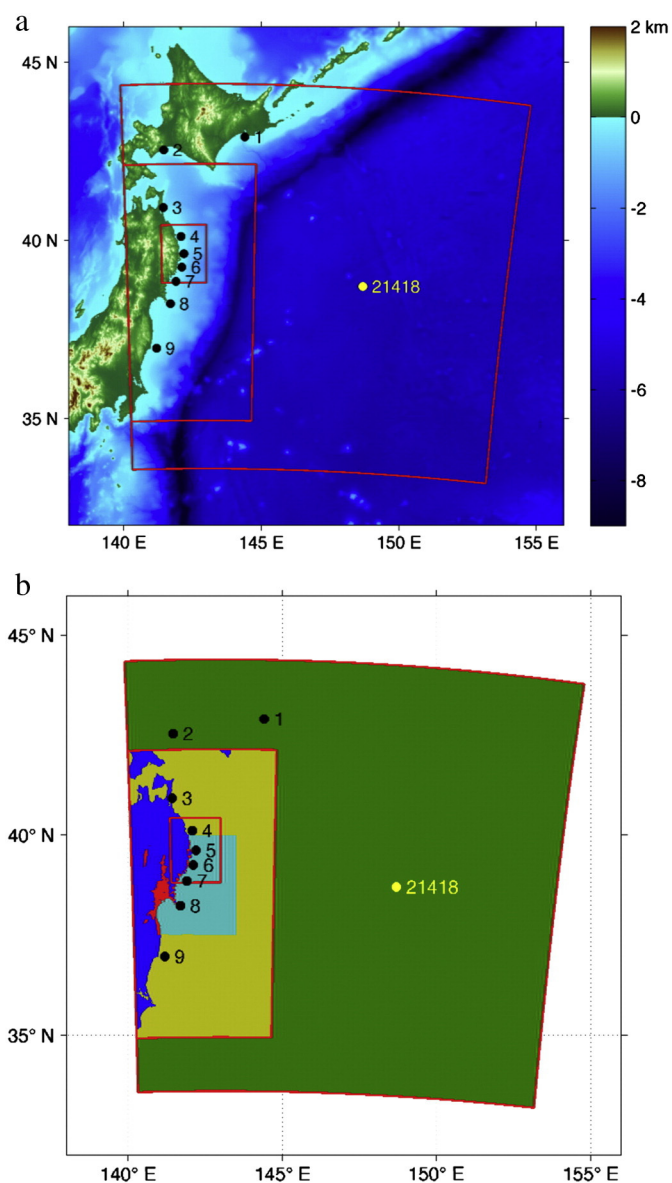

Fig. 8. (a) Computational domain boundaries for simulations with FUNWAVE-TVD (large/medium/small red boxes: 1000/250/50 m grids) and NHWAVE (large red box: 1000 m grid); numbered dots indicate the location of the GPS (black; #1–9) and DART (white; #21418) buoys. (b) Bathymetric and topographic data sources in and around the various computational domains: ASTER—blue (1″ arc data used for topography greater than 100 m elevation or outside of Sanriku region); JODC—ocher (used for bathymetry outside of Sanriku region); JHA—cyan (used for bathymetry in Sanriku region); GSI—red (50 m resolution topography between 0 m and 100 m elevation within Sanriku region); ETOPO-1—green (1′ resolution bathymetry used for 1 km grid). (For interpretation of the references to color in this figure legend, the reader is referred to the web version of this article.)

boundary of finer resolution nested grids include reflected waves as well as incident waves, open boundary conditions are automatically satisfied. Due to the fairly small horizontal extent of NHWAVE's and FUNWAVE-TVD's computational domains (Fig. 8), Cartesian grids are used in both models, with distance corrections applied to account for the Earth's sphericity, based on a transverse secant Mercator projection (similar to the UTM system, with an origin located at 39° N, 143° E). This transformation leads to negligible grid distortions.

The generation of SMF tsunamis in NHWAVE is simulated as a time-dependent seafloor deformation based on specified SMF geometry and kinematics. Both are idealized to represent the small displacement of a rigid rotational SMF (i.e., a slump; see, Grilli and Watts, 1999, 2005; Grilli et al., 2002; Enet and Grilli, 2007), modeled as the center of mass motion $s(t)$ of a volume of sediment V_s moving down a (locally) plane

slope. Such motion is governed by a balance of gravity, inertia, buoyancy, basal and hydrodynamic friction forces. For a rigid slump with constant basal friction and negligible hydrodynamic drag, we find (Grilli and Watts, 2005),

$$
s(t) = \begin{cases} 0 & t < t_i \\ s_0\left(1 - \cos\left\{\dfrac{t - t_i}{t_0}\right\}\right) & t_i \le t < t_i + \pi t_0 \\ 2s_0 & t_i + \pi t_0 \le t \end{cases} \tag{4}
$$

where t_0 and s_0 denote characteristic time and distance of motion. Eq. (4) describes a pendulum-like motion for the slump center of mass. Here, parameters t_i, t_0, and s_0 were all inferred by correlating tsunami observations (i.e., travel time, dominant wavelength and height) with simulations.

As in Enet and Grilli (2007), we idealize SMF geometry as a quasi-Gaussian-shaped volume, whose steepness is controlled by a shape parameter ε, with an elliptical footprint of length b, width w, and thickness Th (Figs. 3, 7 and 9). We similarly use $\varepsilon = 0.717$, which yields a fairly bulky Gaussian shaped volume, that does not taper too much towards its extremities, similar to actual slumps; this is a reasonable choice in the absence of sub-bottom seismic data. With these assumptions, the SMF initial vertical elevation below the pre-earthquake seafloor is modeled as,

$$
\begin{aligned}
\zeta(\xi, \chi) &= \frac{T}{1 - \varepsilon} \max[0, \quad \mathrm{sech}(k_b \xi)\,\mathrm{sech}(k_w \chi) - \varepsilon] \\
k_b &= \frac{2}{b}\,\mathrm{acosh}\frac{1}{\varepsilon} \\
k_w &= \frac{2}{w}\,\mathrm{acosh}\frac{1}{\varepsilon}
\end{aligned} \tag{5}
$$

where (ξ, χ) are the local downslope and span-wise coordinates, rotated to the direction of SMF motion θ (97°clockwise from north; Fig. 9),

$$
\begin{aligned}
\xi &= (x - x_0)\cos\theta - (y - y_0)\sin\theta - s(t) \\
\chi &= (x - x_0)\sin\theta + (y - y_0)\cos\theta
\end{aligned} \tag{6}
$$

with $s(t)$ given by Eq. (4), and (x_0, y_0) the initial SMF center of mass location given by the MBES bathymetry. The SMF absolute displacement parallel to the slope (i.e., runout) is very small (about 1.5%) compared to its estimated length: $s(t_f) = s_f = 2\,s_0 = 300$ m, and is derived iteratively for tsunami simulations to match the recorded higher-frequency waves at the buoys (Fig. 2). The displacement duration $t_f = \pi t_0 = 63$ s is also derived from comparing simulations with buoy data. Because of its large size 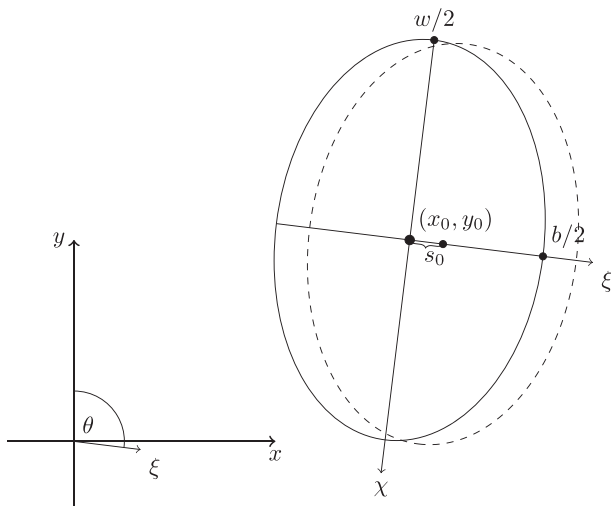compared to runout, the SMF essentially moves as a rigid block. With these parameters, the initial SMF acceleration, $a_0 = s_0/t_0^2 = 0.37$ m/s², together with volume, is a first-order control on the tsunamigenic potential of the SMF (e.g., Grilli and Watts, 2005; Lynett and Liu, 2005 and see also Watts et al., 2005 for a discussion).

The instantaneous seafloor depth above the SMF is given by (with, $\Delta h = h - h_0$),

$$
h(x, y, t) = h_0(x, y) + \zeta\{\xi(x, y), \chi(x, y), t\} - \zeta\{\xi(x, y), \chi(x, y), t_i\} \tag{7}
$$

where $h_0(x, y)$ is the local bathymetry (e.g., Fig. 7). This results in a motion that is nearly equivalent to a translation of part of the seabed parallel to the local average slope. The maximum seafloor uplift caused by the SMF motion for these idealized SMF geometry and kinematics and failure parameters, is $\Delta h = 91$ m (Fig. 7b). The vertical SMF seafloor velocity (used in NHWAVE as a bottom boundary condition) is then computed as

$$
\frac{dh}{dt}(x, y, t) = \frac{d}{dt}\{\zeta\{\xi(x, y, s(t)), \chi(x, y)\}\}, \tag{8}
$$

which can be obtained by differentiation of Eqs. (4)–(7).

Through a series of iterative simulations of the dual source tsunami, we found the SMF-triggering time delay that led to the best match with the observed arrival time of higher-frequency waves at the GPS and DART buoys (Fig. 2) to be $t_i = 135$ s. This timing is consistent with the 110 s delay obtained from tsunami inversion (e.g., Takagawa and Tomita, 2012). It can be explained by the finite time of shear wave propagation from the earthquake hypocenter to the toe of the accretionary prism (Yue and Lay, 2011), and loss of sediment shear strength from liquefaction along the basal décollement that is normal in SMF. SMF motion terminates at $t = t_i + t_f = 198$ s (3.3 min) from the time of earthquake rupture; this total time is identical to the delay independently found from the simplified travel time analysis of Fig. 3. As seen in Fig. 7b, there is downward seafloor displacement at the rear of the SMF and upward at the front, as expected for a rotational failure and confirmed by the post-earthquake bathymetry of the SMF source used (Fig. 5). The free surface elevations of the SMF-generated wave at $t = 300$ s are in the range -10 to 16 m (Figs. 10 and 11). As expected from similar earlier work (e.g., Day et al., 2005; Tappin et al., 2008), at this and later times, the tsunami wave train generated by the SMF located north of the main earthquake rupture, is more directional than waves generated by the earthquake source with, despite the cylindrical pattern of generated waves, higher amplitude waves being generated near the SMF azimuthal direction of motion (axis). The SMF-generated waves also are shorter and higher-frequency (thus more dispersive) than those generated to the south by the earthquake (Figs. 2, 10 and 11). The results of the dual source tsunami are presented as two videos: an overall view of the tsunami (hyperlink to Video 1) and a close-up in the region near the Sanriku Coast (hyperlink to Video 2) (for explanation of video see caption for Fig. 11).

As seen in Eqs. (4)–(8), with our idealized tsunami generation method (Grilli and Watts, 2005), which represents the rigid SMF motion by that of its center of mass, SMF thickness and volume do not play a direct role in kinematics and, therefore, on seafloor motion and SMF tsunami source characteristics. However, as discussed above in the slope stability analysis, SMF thickness and volume affect some of the physical parameters that control sediment failure through sediment stability and thus indirectly the values of runout and failure time, determined through modeling (see below), that control Eq. (4).

Within the constraints of seafloor morphology, the SMF site area and its size (Fig. 5), and reasonable SMF aspect ratios, we refine the SMF source kinematics and time of failure by iteratively modeling tsunami generation for several sets of SMF parameters, together with the UA earthquake source, to better match the tsunami observations. Doing so, we found $s_f = 300$ m (i.e., $s_0 = 150$ m) and $t_f = 63$ s (i.e., $t_0 = 20$ s) and, from these parameters, that the characteristic
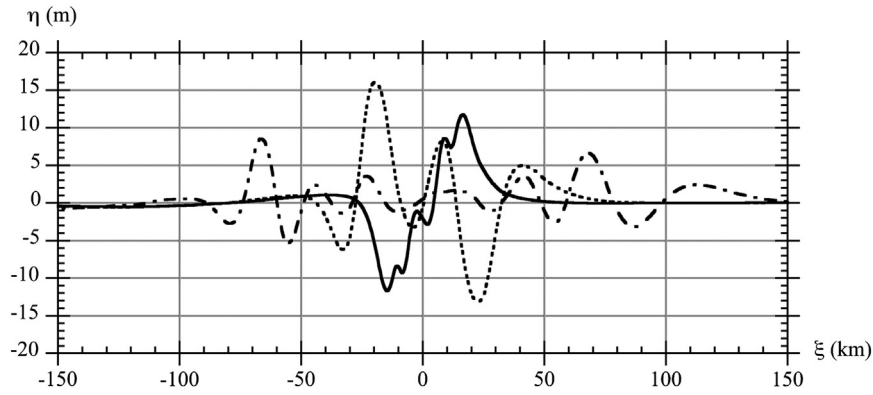

Fig. 9. Geometric parameterization of SMFs moving in transect direction ξ, with an azimuth angle θ from North.

Fig. 10. Sea surface elevation of SMF tsunami generated along transect in azimuthal direction theta = 97° from North, through SMF center of mass location at 39.37° N, 144.00° E (through center of red ellipse and parallel to transects #3 and #4 in Fig. 6), at $t = 198$ s (solid; $t = ti + tf = 3$ min. 18 s); 5 min. (- - - -); 10 min. (- . - . -). ξ is distance from center of motion. Left towards the coast.
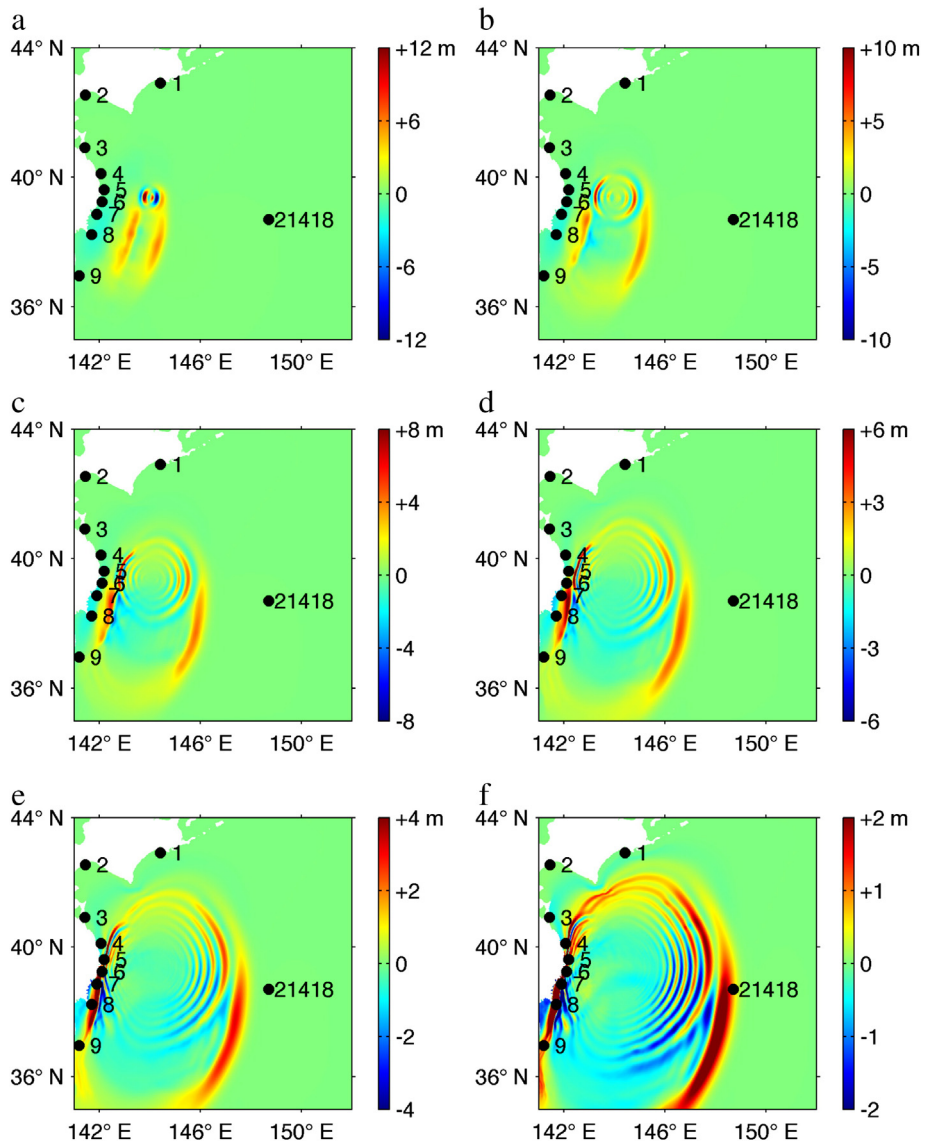

Fig. 11. Results of NHWAVE–FUNWAVE simulations using the UA plus SMF source, showing instantaneous surface elevations at $t =$ (a) 5; (b) 10; (c) 15; (d) 20; (e) 25; (f) 30 min, in the 1 km FUNWAVE grid (Fig. 8a). Labeled black dots mark the locations of GPS buoys and of DART buoy #21418 (time series shown in Fig. 2). Note the highly dispersive nature of waves generated by the SMF source to the north, as compared to the longer wavelength, long-crested, non-dispersive earthquake-generated tsunami waves to the south (A simulation of this figure is shown in Video 1).

wavelength of the generated tsunami was initially on the order of twice the SMF length b, which is as expected, although perhaps slightly larger because of wave propagation during SMF motion (e.g., Fig. 10 for $t = 198$ s). The simulation resulted in leading (onshore propagating) waves generated along the SMF axis with a wavelength $L \approx 40$ km when they reach a depth $h_0 \approx 3$ km (Fig. 10, $\xi = -30$ km; dashed line at $t = 5$ min), while their height (trough to crest) varied proportionally to s_f, and the delayed timing of failure was $t_i = 135$ s. According to linear wave theory (Eq. (1)), these L and h_0 values translate into $T \sim 4$ min period waves, which match the higher-frequency waves observed at the three Iwate GPS buoys (nos. 4–6 in Fig. 1; waveforms in Fig. 2d–f) and DART buoy #21418 (Fig. 2j), which ride over longer, 20–40 min period, earthquake-generated tsunami waves. It should be noted that the iterative tuning of the parameterization of the SMF involves complex tradeoffs between the various parameters.

To accurately simulate nearshore tsunami propagation, runup, and inundation along the Sanriku coast, which has a complex topography with many narrow valleys, we use nested grids of 1000 m, 250 m, and 50 m resolution (Fig. 8a). Bathymetric and topographic data for the coarser grid were derived from the 1 arc-min (1800 m) resolution ETOPO-1 database (Fig. 8b). For the higher resolution grids, bathymetric and topographic data were derived from (Fig. 8b): (i) the 500 m resolution JEGG500 bathymetry (JODC Expert Grid data for Geography) along the entire Japanese coastline; and (ii) the 1″ arc (about 30 m) ASTER topographic data. Offshore of the area of maximum coastal impact from 37.4° N to 40.0° N along the Sanriku coast, additional bathymetric data were obtained from the Japan Hydrographic Association's (JHA) 50 m resolution (M7005) digital maps and topographic data from the Geospatial Information Authority of Japan (GSI). Data sets from the various sources were linearly interpolated. Note that the higher resolution bathymetric and topographic datasets used (ASTER, JHA, GSI) are consistent with the finest resolution grid used in simulations (50 m), and are thus deemed adequate for the present study. Higher resolution simulations of coastal inundation (e.g., using 10–30 m grids, which is standard) could further refine assessments of local tsunami impact but would require both higher resolution data and finer model grids.

8. Validation of the tsunami simulations

We validate our modeling results for the dual (UA plus SMF) source using a number of methods: (i) the results of tsunami propagation simulations (Fig. 11 and videos); (ii) a comparison of simulated tsunami
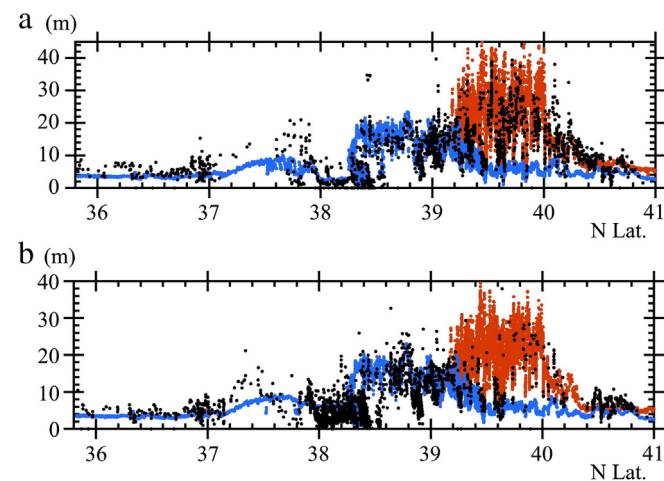

Fig. 12. Tsunami runup and flow depth measured by Mori et al. (2012) in field surveys (black dots). (a) Runup. (b) Inundation/flow depth at the shoreline. Simulations using the UA earthquake source alone (blue line) cannot explain data between about 39° N and 41° N, while the dual UA plus SMF source (red dots) fits the observations to a higher degree. (For interpretation of the references to color in this figure legend, the reader is referred to the web version of this article.)

runup (maximum onshore elevation; Fig. 12a) and inundation (flow depth at the shore and extent of landward penetration; Figs. 12b, 13) with data recorded during post-tsunami field surveys (Mori et al., 2012); (iii) a comparison of simulated and recorded tsunami waveforms (surface elevations) at the GPS and DART buoys (Fig. 14); and (iv) a wavelet analysis of three nearshore GPS buoys and the offshore DART #21418 buoy (Figs. 15–18). To further test the validity of our modeling results we also obtained digital data for synthetic tsunami waveforms that were computed by other authors using different models and methods of tsunami generation, to compare with our synthetics and the observed buoy data (Fig. 19).

8.1. Tsunami simulations

Instantaneous surface elevations computed in model simulations using the 1000 m FUNWAVE grid, for the dual (UA plus SMF) source show the marked differences in the tsunami wavelengths generated from the two sources (time series snapshot images shown in Fig. 11 and a simulation in Video 1). Most notable are the shorter and more onshore-focused, dispersive wave trains generated by the SMF source in the north, compared to the longer wavelength and long-crested, non-dispersive, earthquake-generated tsunami waves to the south. The nature of these waves from still snapshots is emphasized on large-scale (Video 1) and coastal close-up (Video 2) video files of these simulations.

8.2. Onshore field survey data

Tide gauges at the coast were mostly destroyed by the tsunami, so onshore runup and flow depth data were obtained from post-tsunami field surveys (Mori et al., 2012). Tsunami runup (maximum onshore elevation) and inundation (flow depth at the shore and penetration) data were measured at more than 5300 individual locations during post-event surveys along a 2000 km stretch of the Japanese coast. Flow depths were obtained from watermarks on trees, walls, and buildings, and detided for the time of tsunami impact. In the area between 39.2° and 40.4° N, the maximum flow depth and runup elevations computed by the simulations for the dual (UA plus SMF) source are 37 and 45 m respectively, as compared to 6 and 15 m for the earthquake-generated tsunami alone (Fig. 12). In contrast, on the Sendai Plain to the south, the dual-source simulation results do not differ significantly from those for the earthquake-only source, a difference explained by the high directionality of the largest tsunami waves generated by the SMF that results in a high degree of focusing along the central Sanriku coast. The agreement between simulations using the dual (UA plus SMF) source and the field observations is very good along the entire Sanriku coast, unlike the UA earthquake source alone which significantly underpredicts the observations of runup and flow depth in the central area. Similarly, in this area there is again good agreement between the model simulations from the dual (UA plus SMF) source and the measured extent of inundation penetration (Fig. 13).

8.3. Time series analysis

An analysis of the time series of surface elevation observed and simulated at the GPS/DART buoys (Fig. 14) was performed to determine whether the proposed dual (UA plus SMF) source reproduces the timing of the waves and their frequency content at the buoys. We used data from the 9 GPS NOWPHAS (Nationwide Ocean Wave information network for Ports and Harbors; http://nowphas.mlit.go.jp/info_eng.html) buoys moored near the Japan coast, and the offshore DART buoy #21418 (Table 2; Fig. 2; locations marked in Figs. 1, 8 and 11). The NOWPHAS buoys are moored 10–20 km offshore in water depths of 100 to 300 m. The DART buoy is located 600 km offshore in 5700 m water depth. The observed time series of surface elevations were obtained by applying a low-pass filter with a moving average technique (Yamazaki et al., 2011).
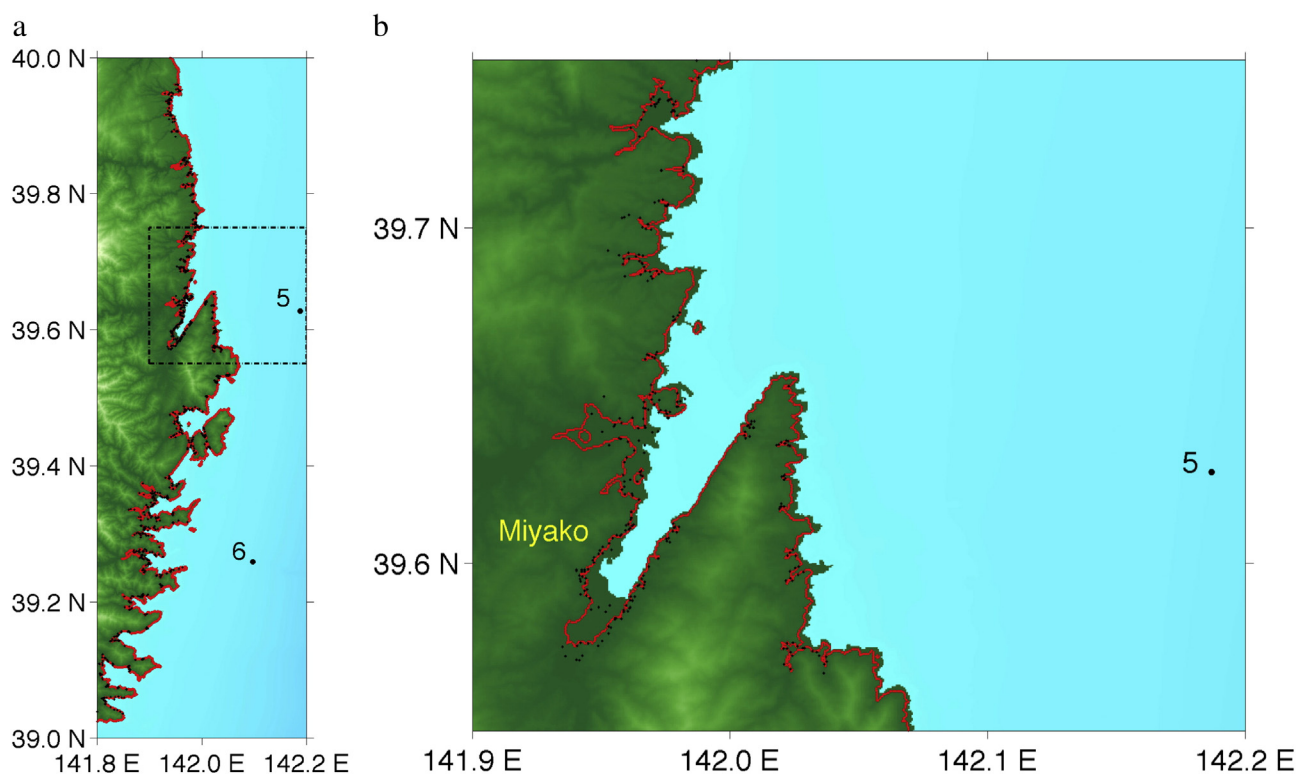
Fig. 13. Tsunami inundation penetration along the Sanriku coast (a: entire; b: zoom around Miyako): measured in field surveys (small black dots); and from model simulations with the dual UA + SMF source (red line). Numbered black dots mark locations of GPS buoys (Fig. 3): (5) Central Iwate; (6) South Iwate. Note that there was a breakwater at the entrance of Miyako Bay (39.65° N) that reduced tsunami inundation (Tomita and Yoem, 2012). Black rectangle in (a) is location of (b). See Video 2 for a simulation of the tsunami inundating this region. (For interpretation of the references to color in this figure legend, the reader is referred to the web version of this article.)

Overall, the dual-source model produces accurate predictions of tsunami elevations measured at the nearshore buoys (Figs. 14a–i), and DART buoy #21418 (Fig. 14j); it is instructive to compare these results with those in Fig. 2 for the UA earthquake source only. The results for the UA seismic source alone and the dual (UA plus SMF) source are nearly identical, except at the three Iwate buoys (Figs. 14d–f) and DART buoy #21418 (Fig. 14j), where the dual (UA plus SMF) source is required to explain the observations. This confirms the highly focused nature of SMF-generated waves along the central part of the Sanriku coast, where the best agreement, between the simulations and the observed data, is clearly obtained from the dual (UA plus SMF) source.

The three central Iwate buoys are located off of the region of the largest coastal runups (from 39.2°–40.4° N) (Fig. 12). The SMF source generates large amplitude, higher-frequency waves (with trough to crest wave heights of 5.3 to 7 m) that ride on the longer wavelength, lower frequency earthquake-generated tsunami waves. The leading, shorter-period, waves of between 3 and 4 min duration are consistent with the SMF characteristic wavelength. Although the periods of the SMF-generated waves are much shorter than those of the dominant, earthquake-generated tsunami (20–40 min), they are comparable in amplitude, although these are even higher at some locations.

At the DART buoy #21418, the simulated wave progression matches the recorded wave sequence reasonably well (Fig. 14j). Because DART buoys use a bottom mounted pressure sensor and compute surface elevation assuming hydrostatic pressure, in the model-data comparison a correction is applied to account for non-hydrostatic (dispersive) effects in shorter wavelength surface waves (for which the water depth to wavelength ratio, $h/L > 1/20$). Specifically, given a computed surface elevation time series $\eta(t)$ in water depth h (i.e., 5700 m for the DART buoy #21418), a Fourier transform is applied to determine the elevation $\hat{\eta}(\omega)$ in the frequency domain. Wavenumbers k are then found for each

frequency from the linear dispersion relationship Eq. (1). The pressure-corrected elevation is found as $\hat{\gamma}'(\omega) = \hat{\eta}(\omega)/\cosh(kh)$. Finally, we apply an inverse Fourier transform to $\hat{\gamma}'(\omega)$, to determine the corrected time series $\eta'(t)$, which are plotted for simulations with various sources and compared to observations (Fig. 14j). The SMF source creates a high-frequency, oscillatory dispersive wave tail (also clearly seen in Fig. 11f), with the period of the highest first wave in the tail approximately 4 min, followed by shorter wavelength and lower amplitude waves.

8.4. Wavelet analysis

For the nearshore GPS buoys North, Central and South Iwate, and DART buoy #21418, we performed a wavelet analysis on the observed and simulated time series of surface elevation, to identify whether a higher-frequency SMF signal was present (Figs. 14 and 15–18). We used the continuous wavelet transform (Farge, 1992) based on a Morlet wavelet, implemented in the frequency domain. Complex wavelet transforms were constructed based on a resampled frequency resolution of 1 Hz for both modeled and recorded signals, and for 500 frequencies evenly spaced in the range $0 < f < 750$ mHz. We separately applied the analysis to simulations using the earthquake UA source and the dual UA plus SMF source, with the SMF triggered at $t = 135$ s. In the recorded data at North Iwate (Fig. 15a) there are two pulses of high-frequency energy; the first at around 0.55 h after the start of the earthquake, with maximum power between 4 and 5 mHz, and the second around 0.90 h with maximum power at a slightly lower frequency of about 3 mHz. These components of the signal are present in the UA plus SMF source (Fig. 15b), where the simulation produces the two distinct high-frequency peaks, with localization in both time and frequency agreeing well with the recorded data, although they are each shifted to slightly lower frequency. They are absent, however, in the simulation based on the UA earthquake source alone (Fig. 15c). Similar results are
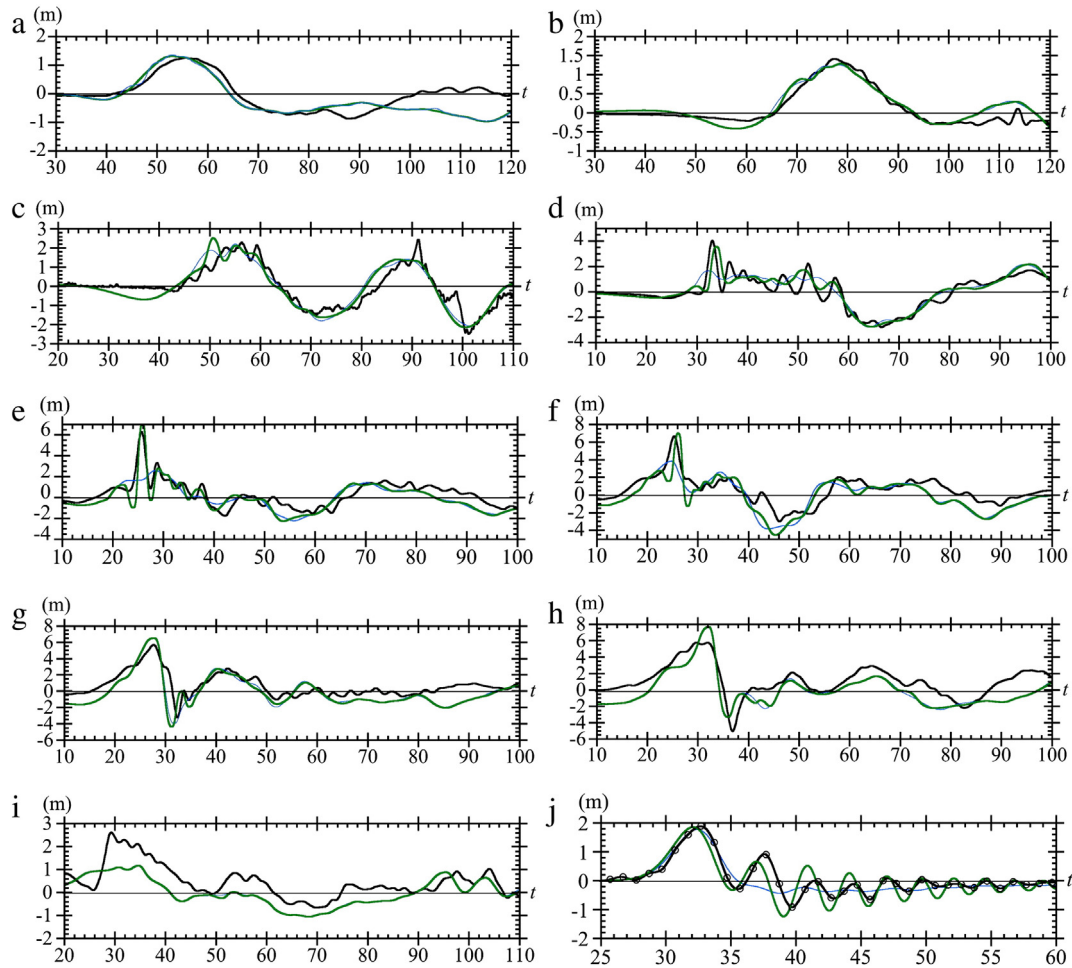
356 *D.R. Tappin et al. / Marine Geology 357 (2014) 344–361*

Fig. 14. Black and light blue curves are recorded data and simulated UA earthquake source results, respectively, at the GPS (a–i) and the DART buoy (j), (locations in Fig. 1 and Table 2). (Note that the black circles in panel j show the actual data points which have been interpolated by a spline curve.) Green curves are results for the dual UA plus SMF source simulation. (For interpretation of the references to color in this figure legend, the reader is referred to the web version of this article.)

also seen at the Central and South Iwate buoys (Figs. 16 and 17), where a single dominant high-frequency peak persists for about 0.2 h. The main elements of the recorded GPS buoy data, therefore, are simulated by the UA plus SMF source (Figs. 15b–17b), but not by the UA earthquake source alone, for which the corresponding high-frequency signal content is absent (Figs. 15c–17c).

In the data recorded at DART buoy #21418 (Fig. 18a) there is a prominent ridge of high-frequency energy, which gradually increases
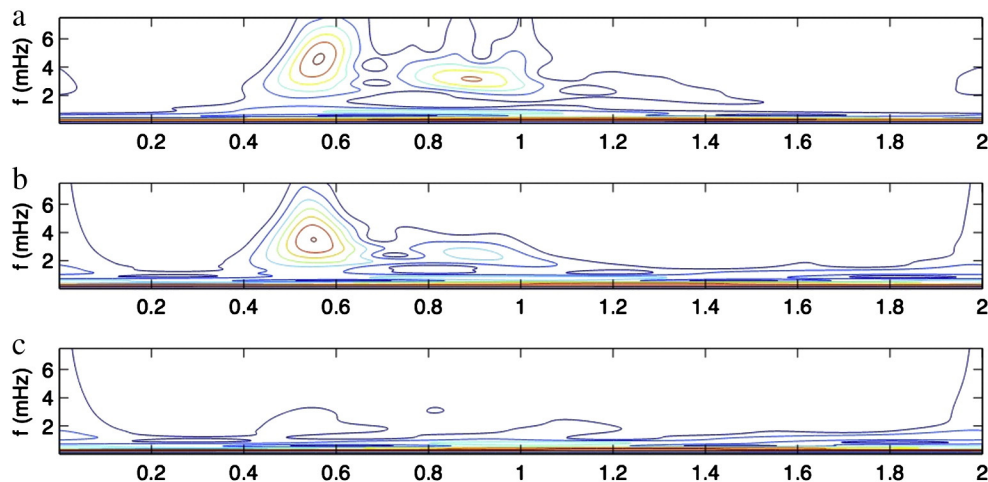

Fig. 15. Modulus of continuous wavelet transform for North Iwate GPS buoy corresponding to time series shown in Fig. 2d (x axis in hours). (a) Observed GPS data, and simulation based on: (b) UA plus SMF source, (c) UA source alone. Location in Fig. 1 and Table 2.
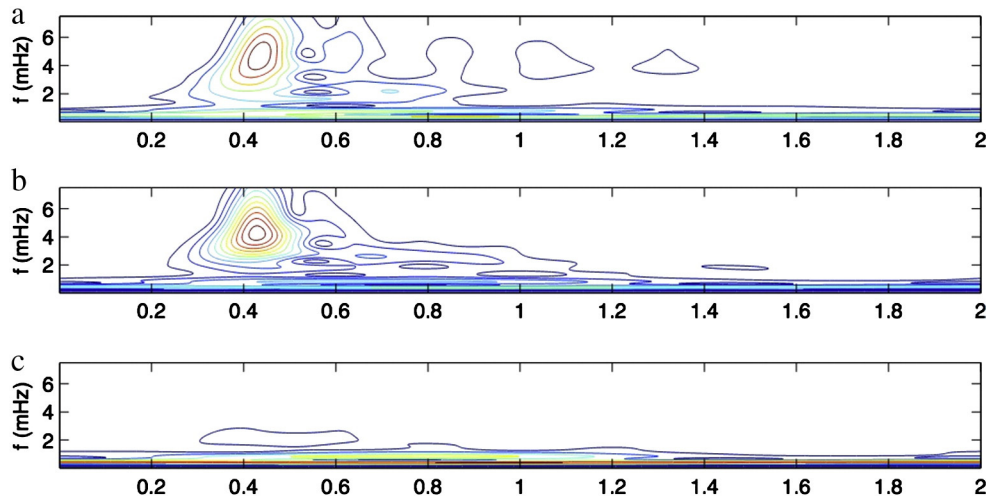
Fig. 16. Modulus of continuous wavelet transform for Central Iwate GPS buoy corresponding to time series shown in Fig. 2e (x axis in hours). (a) Observed GPS data, and simulation based on: (b) UA plus SMF source, (c) UA source alone. Location in Fig. 1 and Table 2.

from 3 to 5 mHz, between 0.55 to 0.65 h after the start of the earthquake. This high-frequency wave signature indicates the presence of a highly dispersive wave train in the signal that cannot be explained by the UA earthquake seismic source alone, where the energy is concentrated at much lower frequencies (Fig. 18c). Only the dual UA plus SMF source (Fig. 18b) captures the structure of this high-frequency dispersive tail, although it is shifted slightly later in time.

Overall, it is clear from this analysis of the buoy data that the considerable amount of energy at frequencies above 3 mHz observed in the recorded data is inconsistent with the UA earthquake source alone. In contrast, the high-frequency signal is simulated relatively well with the addition of the proposed SMF source. For the earthquake UA source the simulated surface elevations uniformly lack high-frequency content above 3 mHz. The absence of this high-frequency content is notable in simulations for GPS buoys facing the Sanriku coast and DART buoy #21418. In contrast, simulated GPS/DART buoy wave elevations for the dual (UA plus SMF) source result in time-frequency signatures which match the observed high-frequency content above 3 mHz and which localize this content correctly in space and time.

8.5. Comparison with synthetics for other models

We compare both our synthetic waveforms (blue lines) for the dual (UA plus SMF) source and those computed by four other studies to observed data (black lines) at the three Iwate GPS buoys and DART buoy #21418 (Fig. 19). The four other studies are (i) Iinuma et al. (2012; yellow lines), whose model is based on the seafloor displacement field calculated from the estimated seismic interplate slip distribution; (ii) Gusman et al. (2012; green lines) whose model is based on a joint inversion using a combination of tsunami waveforms, GPS data and seafloor crustal deformation data (the crustal deformation is based on a model from Tanioka and Seno, 2001); (iii) Romano et al. (2012; red/brown lines) who use a joint inversion of earthquake-only rupture from static on- and offshore geodetic data in combination with on- and offshore tsunami waveform data (they adjust the offshore GPS buoy data to fit the first higher-frequency waveform peaks recorded at the Iwate buoys); and (iv) Satake et al. (2013; purple lines), whose model was obtained by inversion of onshore GPS data and tsunami waveforms at offshore buoys.

As we already illustrated in panels d–f and j of Fig. 14, the synthetics for our dual source model fit both the initial pulse and the later high-frequency arrivals at these four stations. By contrast, from Fig. 19 it can be seen the synthetics of Iinuma et al. (2012) do not fit the first pulse at any of the three GPS buoys; they fit the first pulse at the DART buoy to some extent, but not the later high-frequency arrivals. The synthetics for the other three studies have large components of very high-frequency noise at the three GPS stations, but these are not present in the observed data. (Note that Gusman et al. did not compute
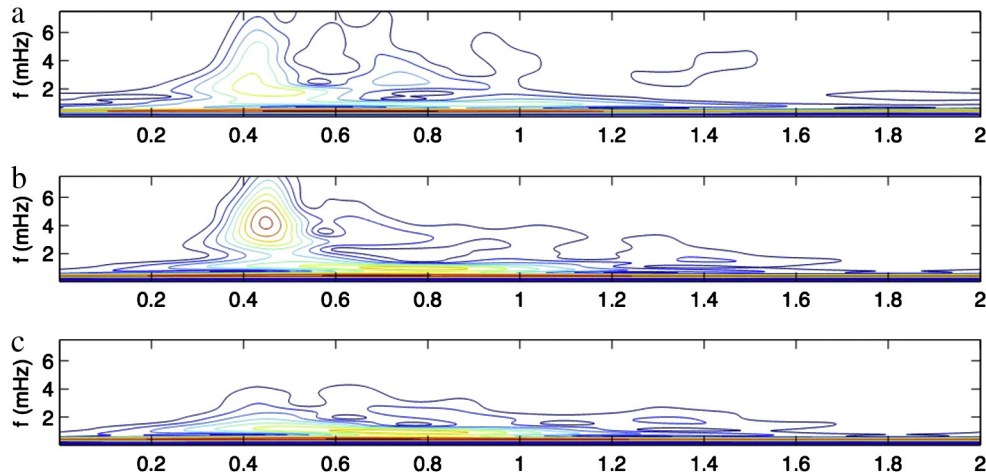

Fig. 17. Modulus of continuous wavelet transform for South Iwate GPS buoy corresponding to time series shown in Fig. 2f (x axis in hours). (a) Observed GPS data, and simulation based on: (b) UA plus SMF source, (c) UA source alone. Location in Fig. 1 and Table 2.
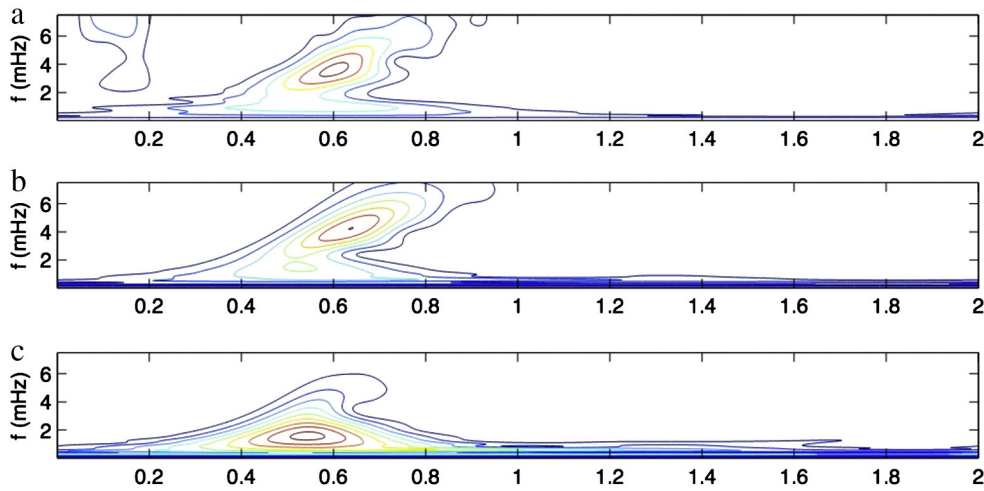
Fig. 18. Modulus of continuous wavelet transform for DART buoy #21418 corresponding to time series shown in Fig. 2j (x axis in hours). (a) Observed GPS data, and simulation based on: (b) UA plus SMF source, (c) UA source alone. Location in Fig. 1 and Table 2.

a synthetic for Iwate North, in panel a). The red/brown trace (Romano et al., 2012) and purple trace (Satake et al., 2013) fit the first two cycles of the data well in panel d of Fig. 19, but the green trace (Gusman et al., 2012) does not.

9. Estimation of seismic wave generation by the SMF from Centroid Single Force (CSF) strength

Our estimated SMF has a volume on the order of 500 km³ and hence one should ask whether seismic waves generated by the SMF could have been detected within the larger seismic waves caused by the earthquake. The centroid single force (CSF), as defined by Kawakatsu (1989), is the equivalent body force for an SMF or other landslide source, just as the moment tensor gives the equivalent body force for slip on a fault plane. Comparing the CSF amplitude to the scalar moment can be used to roughly quantify the relative amplitude of the seismic waves generated by the SMF, as compared to those generated by the earthquake. The scalar strength of an SMF source is characterized by its CSF defined as

$$CSF = \rho_s V_s s_f, \tag{9}$$

where ρ_s denotes the sediment bulk density, V_s the SMF volume, and s_f, the SMF runout (or distance traveled).

Our proposed SMF tsunami source, as discussed above, has an assumed elliptical footprint on the seafloor (Fig. 9) of width $w = 40$ km and downslope length $b = 20$ km; runout is $s_f = 300$ m over a time $t_f = 63$ s. The SMF is assumed to have a Gaussian (axisymmetric) shape defined by Eq. (5), with shape parameter $\varepsilon = 0.717$; hence SMF volume is given by, $V_s = 0.2983\ b\ w\ Th$ (Enet and Grilli, 2007). While the SMF footprint can be estimated with relatively good accuracy, based on the ray tracing and geological analyses, as indicated above, the SMF thickness is subject to a larger uncertainty; based on geology, we estimate it could range between $Th = 700$ to 2000 m, which for the maximum thickness, yields a volume $V_s = 477.3$ km³. The bulk density obtained from cores in the region is $\rho_s = 1500$ kg/m³; thus Eq. (9) yields a scalar $CSF = (0.7–2.15)\ 10^{17}$ kg m. As indicated above, the center of the SMF is at 39.37° N and 144.00° E, and the slump moves in azimuthal direction $+97°$ from north (so the CSF vector is $−83°$ from north), down a slope of about 1:15 or 3.81°, so the force vector is opposite.

The CSF calculated here is 2–3 times less than the value calculated for the Kalapana slide by Kawakatsu (1989), but the Tohoku earthquake's scalar seismic moment is about 200 times larger than

that reported for the Kalapana M7.2 earthquake. So, whereas long-period seismic waves generated by the present SMF could have been on the same order of magnitude as those for the Kalapana slide, they would have been much smaller than seismic waves generated by the Tohoku earthquake, as compared to the Kalapana earthquake. It thus seems clear that whereas the SMF is found to have a significant effect in enhancing tsunami amplitudes in northernmost Tohoku, it will not have a significant effect on seismic or geodetic observations, although its effects might be detectable through a detailed study of seismograms recorded at observatories in the Sanriku region.

10. Conclusions

The source of the exceptionally high tsunami runups of up to 40 m recorded along the central Sanriku coast between 39.2° N and 40.2° N on March 11, 2011 has not previously been satisfactorily explained. Here we demonstrate that these high runups can be accounted for by an additional tsunami source, namely an SMF located almost directly east of the central Sanriku coast (Figs. 4 and 12). The SMF contributes to high runups, and extensive inland penetration and inundation (Fig. 13). Along the central Sanriku coast, the tsunami runup and inundation generated by the dual (UA plus SMF) source also reproduce the field observations quite well, whereas the UA seismic source alone severely underpredicts them (Fig. 12). This coast has many deep and narrow valleys of complex topography, which likely amplified the tsunami impact. Hence, in this area, it might have been desirable to use an even finer nested grid level than the 50 m grid, perhaps a 20–30 m grid; but unfortunately no higher resolution topographic data were available to us. Notwithstanding, we compared separate simulations, in the same nested grid system, of tsunami generation and coastal impact for the UA seismic source alone and the dual (UA plus SMF) source, to inundation and runup observations (Fig. 12). These comparisons showed that results for the dual source predict inundation and runup in Sanriku quite well, whereas results for the earthquake-only source do not, confirming the validity of using the 50 m resolution grid of the present study to illustrate the requirement of the proposed SMF to explain the tsunami impact along the central Sanriku coast.

Our modeling of tsunami waveform data at offshore GPS buoys and the DART buoy shows that the observed higher-frequency waves can be best explained by a combination from our SMF triggered with a 135 s delay, a time consistent with the propagation of seismic waves from the main rupture area, and longer waves generated from an earthquake with a main rupture farther south (Figs. 2 and 14). The backward travel time analysis of the high-frequency component of the waveforms
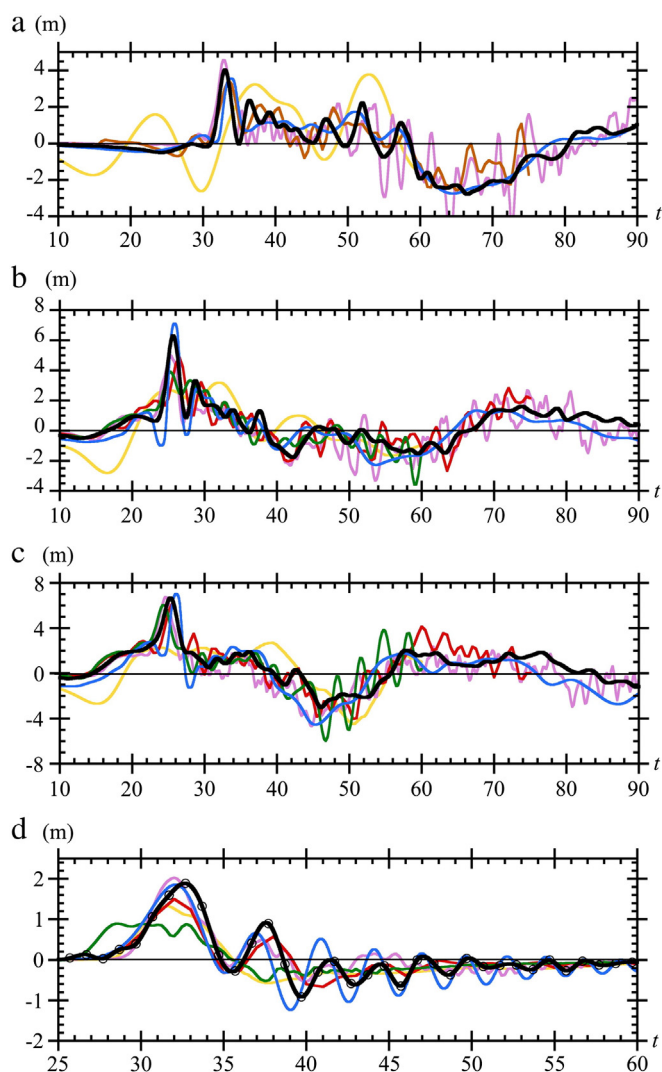
Fig. 19. Simulated and recorded surface elevations at buoys near Japan as a function of time, with simulations from earthquake rupture derived from seismic, geodetic and/or tsunami waveform inversion. (a, b and c) are North, Middle and South Iwate buoys, respectively, and (d) is DART buoy #21418 (see Table 2 and Fig. 1 for buoy locations). Black line is recorded data. (Note that the black circles in panel d show the actual data points which have been interpolated by a spline curve.) Blue line is for dual (UA plus SMF) model presented in this paper. Green line (not shown in panel a) is a joint inversion from tsunami waveforms, GPS data and seafloor crustal deformation (Gusman et al., 2012). Yellow line is from seafloor displacement field calculated from the estimated seismic interplate slip distribution (Iinuma et al., 2012). Red/brown line is a joint inversion of tsunami waveform data and GPS earthquake rupture (Romano et al., 2012). Purple line is from waveform inversion (Satake et al., 2013). (For interpretation of the references to color in this figure legend, the reader is referred to the web version of this article.)

recorded at the GPS/DART buoys identified the most likely SMF tsunami source (Fig. 3). A simplified slope stability analysis confirmed that the SMF could have failed by earthquake loading (Fig. 6). The comprehensive dataset of MBES bathymetry in the vicinity of the earthquake rupture and offshore of the tsunami-inundated coastline validated the presence of a large SMF (of up to ~500 km³) at the location estimated from the travel time analysis, with vertical motions on the order of 100 m, consistent with an SMF failing as a rigid slump with a short runout (Figs. 4 and 5). On the bathymetry, near our source SMF we also identify a number of other large-scale SMFs, but these pre-date the 2011 earthquake (Fig. 4).

Comparison of the observed wave elevations at near and offshore buoys near Japan with our group's tsunami simulations for an earthquake-only source (Grilli et al., 2013) as a function of time

(Fig. 14), and by wavelet analysis (Figs. 15–18) demonstrates that the tsunami from the earthquake-only source cannot generate the high-frequency components seen in the observed data (Fig. 2). These high-frequency components, however, can be reproduced by an SMF located at the northern boundary of the earthquake rupture zone, as identified by the backward ray tracing. Comparison of our simulations for the dual source with those for other published models based only on an earthquake source, or ones somewhat modified, demonstrates that the dual source is more successful in reproducing the high-frequency components of the observed GPS and DART buoy data (Fig. 19). The CSF results reveal that the proposed SMF, despite its large size, would not have caused a large seismic signal, as compared to the much larger seismic waves generated by the earthquake. So, the presence or absence of an SMF source would not significantly affect the seismic data.

11. Implications for hazard estimation

Our results have important broader implications for the mechanism of tsunami generation, both in Japan along the Tohoku coast, and elsewhere (Harbitz et al., 2013; Wei et al., 2014). Anomalous tsunamis, with 40 m runups focused along a narrow coastal corridor, have occurred in the past in Tohoku, most notably the Great Meiji tsunami of 1896 in which 26,000 people perished. This tsunami has been attributed to a slow "tsunami" earthquake (Tanioka and Seno, 2001) or to large-scale slip near the trench axis (Tanioka and Satake, 1996). On the basis of our results, however, we suggest that this event may have been caused, at least locally, by an SMF, as proposed previously by Tanioka and Seno (2001). In the MCS lines off of Sanriku shown by Tsuru et al. (2002, e.g., Figs. 4 and 6) there are numerous SMFs that correlate with many of the slumps mapped from MBES in our Fig. 4. Some of these SMFs are near the inferred rupture area of the 1896 earthquake (Tanioka and Satake, 1996). Significantly, there are reports that for the 1896 event, the sea initially withdrew, and that the tsunami had a leading depression wave; both observations supporting the possibility of a tsunami generated in large part by an SMF (Grilli and Watts, 2005). The initial Tohoku 2011, earthquake-generated, tsunami wave was positive with two pulses (Fujii et al., 2011; Maeda et al., 2011) and inundated the Sendai coast as a surge (Tappin et al., 2012). As we show in our dual source modeling (Figs. 11 and 12), both the earthquake- and SMF-generated waves would arrive near the shore almost simultaneously, thus their combined elevations impacting the coast together would explain an absence of an initial ocean drawdown and sea withdrawal despite the SMF component.

Evidence for large-scale SMFs is only seen off the northeast Pacific Coast of Honshu Island (Figs. 1 and 4). This concentration suggests a major, and insufficiently appreciated, tsunami hazard from SMF in this region. Along other convergent margins, few hazardous SMF-sourced tsunamis have as yet been definitely proven, although there is strong evidence for dual, earthquake-SMF events in Alaska, 1946 (Fryer et al., 2004), Flores Island, 1994 (Tsuji et al., 1995) and Java, 2006 (Fritz et al., 2007). One definite recent example, however, is the 1998 Papua New Guinea tsunami (Tappin et al., 2001, 2008; Synolakis et al., 2002), where a delayed, earthquake-triggered, submarine slump caused 2200 deaths from a tsunami with maximum coastal flow depths of 16 m, and a focused runup along a limited length of coast. The identification in the present study of the 2011 Tohoku event of a second major SMF-generated tsunami, especially one associated with a M9 earthquake, is therefore important in guiding future research that contributes to the improved forecasting and mitigation of the tsunami hazard from large megathrust plus SMF events, both in Tohoku and globally. It seems highly likely that the other large SMFs we identified on the MBES data off Sanriku could have generated significant tsunamis and therefore should be considered in analyses of the tsunami hazard in Japan. Our results also suggest a potential pitfall in the use of tsunami waveform inversion from tide gauges and buoys to estimate the size and spatial characteristics of earthquake rupture. If the tsunami source has a

significant SMF component such studies may over-estimate the magnitude of the earthquake. It also would be desirable to extend real-time tsunami warning systems (e.g., Gusman and Tanioka, 2014) to include the effects of SMFs, although realizing this goal will involve formidable technical challenges.

The question of how future earthquake hazards should be estimated in general remains open. Thirty or forty years ago it was widely believed that "characteristic earthquakes" occurred more or less periodically, and that this could be used as the basis for making hazard estimates. However, statistical tests have refuted the characteristic earthquake hypothesis (Kagan et al., 2012) and hazard maps made using the characteristic earthquake hypothesis fail to agree with subsequent seismicity (Stein et al., 2012), so it appears that new methods are required. As for the past tsunami history in Tohoku, a paleo-tsunami study by Minoura et al. (2001) found that in addition to the very large tsunami in 869 (during the "Jogan era," in Japanese history), the Sendai Plain had also experienced two other similar tsunamis in the past 3000 years. The size of these three tsunamis was generally comparable to that of the 2011 event (Mori et al., 2012). Paleo-tsunami studies further to the north have not been made, due mainly to the lack of preserved tsunami deposits, so the spatial extent of the Jogan event and the two earlier events found by Minoura et al. (2001) remains unclear. The need for new approaches to hazard estimation, the uncertainties regarding the past events, and the possibility of SMF-generated secondary tsunamis are all challenges that must be addressed in future studies.

Acknowledgments

Appendix A. Supplementary data

Supplementary data associated with this article can be found in the online version, at http://dx.doi.org/10.1016/j.margeo.2014.09.043.

References

Abadie, S., Morichon, D., Grilli, S.T., Glockner, S., 2010. Numerical simulation of waves generated by landslides using a multiple-fluid Navier–Stokes model. Coastal Engineering 57, 779–794. http://dx.doi.org/10.1016/j.coastaleng.2010.03.003.

Ammon, C.J., Lay, T., Kanamori, H., Cleveland, M., 2011. A rupture model of the 2011 off the Pacific coast of Tohoku Earthquake. Earth, Planets and Space 63, 693–696.

Bishop, A.W., 1955. The use of the slip circle in the stability analysis of slopes. Geotechnique 5, 7–17.

Cadet, J.P., et al., 1987. The Japan Trench and its juncture with the Kuril Trench: cruise results of the Kaiko project, Leg 3. Earth and Planetary Science Letters 83, 267–284.

Chen, Q., Kirby, J.T., Dalrymple, R.A., Kennedy, A.B., Chawla, A., 2000. Boussinesq modeling of wave transformation, breaking and runup. II: Two horizontal dimensions. Journal of Waterway, Port, Coastal, and Ocean Engineering 126, 48–56.

Chen, Q., Kirby, J.T., Dalrymple, R.A., Shi, F., Thornton, E.B., 2003. Boussinesq modeling of longshore currents. Journal of Geophysical Research 108, 3362. http://dx.doi.org/10.1029/2002JC001308.

Day, S.J., Watts, P., Grilli, S.T., Kirby, J.T., 2005. Mechanical models of the 1975 Kalapana, Hawaii earthquake and tsunami. Marine Geology 215, 59–92.

Dean, R.G., Dalrymple, R.A., 1984. Water Wave Mechanics for Engineers and Scientists. Prentice Hall.

Enet, F., Grilli, S.T., 2007. Experimental study of tsunami generation by three-dimensional rigid underwater landslides. Journal of Waterway Port, Coastal, and Ocean Engineering 133, 442–454.

Farge, M., 1992. Wavelet transforms and their applications to turbulence. Annual Review of Fluid Mechanics 24, 395–457.

Fritz, H.M., Kongko, W., Moore, A., McAdoo, B., Goff, J., Harbitz, C., Uslu, B., Kalligeris, N., Suteja, D., Kalsum, K., Titov, V., Gusman, A., Latief, H., Santoso, E., Sujoko, S., Djulkarnaen, D., Sunendar, H., Synolakis, C., 2007. Extreme runup from the 17 July 2006 Java tsunami. Geophysical Research Letters 34 (L12602).

Fryer, G.J., Watts, P., Pratson, L.F., 2004. Source of the great tsunami of 1 April 1946: a landslide in the upper Aleutian forearc. Marine Geology 203, 201–218.

Fuhrman, D.R., Madsen, P.A., 2009. Tsunami generation, propagation, and run-up with a high-order Boussinesq model. Coastal Engineering 56, 747–758.

Fujii, Y., Satake, K., Sakai, S., Shinohara, M., Kanazawa, T., 2011. Tsunami source of the 2011 off the Pacific coast of Tohoku, Japan earthquake. Earth, Planets and Space 63, 815–820.

Fujiwara, T., Kodaira, S., No, T., Kaiho, Y., Takahashi, N., Kaneda, Y., 2011. The 2011 Tohoku earthquake: displacement reaching the trench axis. Science 334, 1240.

Glimsdal, S., Pedersen, G.K., Harbitz, C.B., Løvholt, F., 2013. Dispersion of tsunamis: does it really matter? Natural Hazards and Earth System Sciences 13, 1507–1526.

Grilli, S.T., Watts, P., 1999. Modeling of waves generated by a moving submerged body. Applications to underwater landslides. Engineering Analysis with Boundary Elements 23, 645–656.

Grilli, S.T., Watts, P., 2005. Tsunami generation by submarine mass failure Part I: Modeling, experimental validation, and sensitivity analysis. Journal of Waterway, Port, Coastal and Ocean Engineering 131, 283–297.

Grilli, S.T., Vogelmann, S., Watts, P., 2002. Development of a 3D numerical wave tank for modeling tsunami generation by underwater landslides. Journal of Waterway, Port, Coastal and Ocean Engineering 26, 301–313.

Grilli, S.T., Ioualalen, M., Asavanant, J., Shi, F., Kirby, J.T., Watts, P., 2007. Source constraints and model simulation of the December 26, 2004 Indian Ocean tsunami. Journal of Waterway, Port, Coastal and Ocean Engineering 133, 414–428.

Grilli, S.T., Dubosq, S., Pophet, N., Pérignon, Y., Kirby, J.T., Shi, F., 2010. Numerical simulation and first-order hazard analysis of large co-seismic tsunamis generated in the Puerto Rico trench: near-field impact on the North shore of Puerto Rico and far-field impact on the US East Coast. Natural Hazards and Earth System Sciences 10, 2109–2125.

Grilli, S.T., Harris, J.C., Tajalli Bakhsh, T.S., Masterlark, T.L., Kyriakopoulos, C., Kirby, J.T., Shi, F., 2013. Numerical simulation of the 2011 Tohoku tsunami based on a new transient FEM co-seismic source: comparison to far- and near-field observations. Pure and Applied Geophysics 170, 1333–1359.

Gusman, A.R., Tanioka, Y., 2014. W phase inversion and tsunami inundation modeling for tsunami early warning: Case study for the 2011 Tohoku event. Pure and Applied Geophysics 171, 1409–1422.

Gusman, A.R., Tanioka, Y., Sakai, S., Tsushima, H., 2012. Source model of the great 2011 Tohoku earthquake estimated from tsunami waveforms and crustal deformation data. Earth and Planetary Science Letters 341–344, 234–242.

Harbitz, C.B., Løvholt, F., Bungum, H., 2013. Submarine landslide tsunamis: how extreme and how likely ? Natural Hazards http://dx.doi.org/10.1007/s11069-013-0681-3.

Hayashi, Y., Tsushima, H., Hirata, K., Kimura, K., Maeda, K., 2011. Tsunami source area of the 2011 off the Pacific coast of Tohoku earthquake determined from tsunami arrival times at offshore observation stations. Earth, Planets and Space 63, 809–813.

Hayes, G., 2011. Rapid source characterization of the 2011 M_w 9.0 off the Pacific coast of Tohoku earthquake. Earth, Planets and Space 63, 529–534.

Horrillo, J., Kowalik, Z., Shigihara, Y., 2006. Wave dispersion study in the Indian Ocean-tsunami of December 26, 2004. Marine Geodesy 29, 149–166.

Ichihara, H., Hamano, Y., Baba, K., Kasaya, T., 2013. Tsunami source of the 2011 Tohoku earthquake detected by an ocean-bottom magnetometer. Earth and Planetary Science Letters 382, 117–124.

Ide, S., Baltay, A., Beroza, G.C., 2011. Shallow dynamic overshoot and energetic deep rupture in the 2011 Mw 9.0 Tohoku-Oki earthquake. Science 332, 1426–1429.

Iinuma, T., Hino, R., Kido, M., Inazu, D., Osada, Y., Ito, Y., Ohzono, M., Tsushima, H., Suzuki, S., Fujimoto, H., Miura, S., 2012. Coseismic slip distribution of the 2011 off the Pacific Coast of Tohoku Earthquake (M9.0) refined by means of seafloor geodetic data. Journal of Geophysical Research 117. http://dx.doi.org/10.1029/2012JB009186 (B07409).

Ioualalen, M., Asavanant, J., Kaewbanjak, N., Grilli, S.T., Kirby, J.T., Watts, P., 2007. Modeling the 26th December 2004 Indian Ocean tsunami: case study of impact in Thailand. Journal of Geophysical Research 112. http://dx.doi.org/10.1029/2006JC003850 (C07024).

Ito, Y., Tsuji, T., Osada, T., Kido, M., Inazu, D., Hayashi, Y., Tsushima, H., Hino, R., Fujimoto, H., 2011. Frontal wedge deformation near the source region of the 2011 Tohoku-Oki earthquake. Geophysical Research Letters 38. http://dx.doi.org/10.1029/2011GL048355 (L00G05).

JAMSTEC, 2011. YOKOSUKA Cruise Report YK11-E06 Leg 1, Japan Agency for Marine-Earth Science and Technology. JAMSTEC; July 11 2011–July 28 2011. (56 pp.,

http://www.godac.jamstec.go.jp/catalog/data/doc catalog/media-/YK11-E06 leg1 all.pdf.

Kagan, Y.Y., Jackson, D.D., Geller, R.J., 2012. Characteristic earthquake model, 1884–2011, R.I.P. Seismological Research Letters 83, 951–953.

Kanamori, H., 1972. Mechanism of tsunami earthquakes. Physics of the Earth and Planetary Interiors 6, 346–359.

Kanamori, H., Kikuchi, M., 1993. The 1992 Nicaragua earthquake: a slow tsunami earthquake associated with subducted sediments. Nature 361, 714–716.

Kawakatsu, H., 1989. Centroid single force inversion of seismic waves generated by landslides. Journal of Geophysical Research 94, 12363–12374.

Kawamura, K., Sasaki, T., Kanamatsu, T., Sakaguchi, A., Ogawa, Y., 2012. Large submarine landslides in the Japan Trench: a new scenario for additional tsunami generation. Geophysical Research Letters 39. http://dx.doi.org/10.1029/2011GL050661 (L05308).

Kawamura, K., Laberg, J.S., Kanamatsu, T., 2014. Potential tsunamigenic submarine landslides in active margins. Marine Geology 356, 44–49.

Kennedy, A.B., Chen, Q., Kirby, J.T., Dalrymple, R.A., 2000. Boussinesq modeling of wave transformation, breaking, and run-up. I: 1D. Journal of Waterway, Port, Coastal and Ocean Engineering 126, 39–47.

Kirby, J.T., Shi, F., Tehranirad, B., Harris, J.C., Grilli, S.T., 2013. Dispersive tsunami waves in the ocean: model equations and sensitivity to dispersion and Coriolis effects. Ocean Modelling 62, 39–55.

Koketsu, K., Yokota, Y., Nishimura, N., Yagi, Y., Miyazaki, S., Satake, K., Fujii, Y., Miyake, H., Sakai, S., Yamanaka, Y., Okada, T., 2011. A unified source model for the 2011 Tohoku earthquake. Earth and Planetary Science Letters 310, 480–487.

Kowalik, Z., Murty, T.S., 1993. Numerical Modeling of Ocean Dynamics. World Scientific.

Kyriakopoulos, C., Masterlark, T., Stramondo, S., Chini, M., Bignami, C., 2013. Coseismic slip distribution for the Mw9 2011 Tohoku-Oki earthquake derived from 3-D FE modeling. Journal of Geophysical Research 118, 3837–3847. http://dx.doi.org/10.1002/jgrb.50265.

Lay, T., Ammon, C.J., Kanamori, H., Xue, L., Kim, M.J., 2011. Possible large near-trench slip during the 2011 Mw 9.0 off the Pacific coast of Tohoku Earthquake. Earth, Planets and Space 63, 687–692.

Løvholt, F., Pedersen, G., Gisler, G., 2008. Oceanic propagation of a potential tsunami from the La Palma Island. Journal of Geophysical Research 113. http://dx.doi.org/10.1029/2007JC004603 (C09026).

Løvholt, F., Kaiser, G., Glimsdal, S., Scheele, L., Harbitz, C.B., Pedersen, G., 2012. Modeling propagation and inundation of the 11 March 2011 Tohoku tsunami. Natural Hazards 12, 1017–1028.

Lynett, P., Liu, P.L.-F., 2005. A numerical study of the run-up generated by three dimensional landslides. Journal of Geophysical Research 110. http://dx.doi.org/10.1029/2004JC00244 (C03006).

Ma, G., Shi, F., Kirby, J.T., 2012. Shock-capturing non-hydrostatic model for fully dispersive surface wave processes. Ocean Modelling 43–44, 22–35.

Ma, G., Shi, F., Kirby, J.T., 2013. Numerical simulation of tsunami waves generated by deformable submarine landslides. Ocean Modelling 69, 146–165.

MacInnes, B.T., Gusman, A.R., LeVeque, R.J., Tanioka, Y., 2013. Comparison of earthquake source models for the 2011 Tohoku event using tsunami simulations and near-field observations. Bulletin of the Seismological Society of America 103, 1256–1274.

Maeda, T., Furumura, T., Sakai, S., Shinohara, M., 2011. Significant tsunami observed at ocean-bottom pressure gauges during the 2011 off the Pacific coast of Tohoku Earthquake. Earth, Planets and Space 63, 803–808.

Masterlark, T., Hughes, K., 2008. Next generation of deformation models for the 2004 M9 Sumatra–Andaman earthquake. Geophysical Research Letters 35. http://dx.doi.org/10.1029/2008GL035198 (L19310).

Minoura, K., Imamura, F., Sugawara, D., Kono, Y., Iwashita, T., 2001. The 869 Jogan tsunami deposit and recurrence interval of large-scale tsunami on the Pacific coast of northeast Japan. Journal of Natural Disaster Science 23, 83–88 (Available at: http://jsnds.org/contents/jnds/list.html).

Miyazaki, S., McGuire, J.J., Segall, P., 2011. Seismic and aseismic fault slip before and during the 2011 off the Pacific coast of Tohoku Earthquake. Earth, Planets and Space 63, 637–642.

Mori, N., Takahashi, T., 2011 Tohoku earthquake tsunami joint survey group, 2012. Nationwide post-event survey and analysis of the 2011 Tohoku earthquake tsunami. Coastal Engineering Journal 54, 1250001. http://dx.doi.org/10.1142/S0578563412500015.

Nettles, M., Ekström, G., Koss, H.C., 2011. Centroid-moment-tensor analysis of the 2011 off the Pacific coast of Tohoku Earthquake and its larger foreshocks and aftershocks. Earth, Planets and Space 63, 519–523.

Ozawa, S., Nishimura, T., Suito, H., Kobayashi, T., Tobita, M., Imakiire, T., 2011. Coseismic and postseismic slip of the 2011 magnitude-9 Tohoku earthquake. Nature 475, 373–376.

Romano, F., Piatanesi, A., Lorito, S., D'Agostino,, N., Hirata, K., Atzori, S., Yamazaki, Y., Cocco, M., 2012. Clues from joint inversion of tsunami and geodetic data of the 2011 Tohoku-oki earthquake. Scientific Reports. 2, 385. http://dx.doi.org/10.1038/srep00385.

Satake, K., 1995. Linear and nonlinear computations of the 1992 Nicaragua earthquake tsunami. Pure and Applied Geophysics 144, 455–470.

Satake, K., Kanamori, H., 1991. Use of tsunami waveforms for earthquake source study. Natural Hazards 4, 193–208.

Satake, K., Fujii, Y., Harada, T., Namegaya, Y., 2013. Time and space distribution of coseismic slip of the 2011 Tohoku earthquake as inferred from tsunami waveform data. Bulletin of the Seismological Society of America 103, 1473–1492.

Sato, M., Ishikawa, T., Ujihara, N., Yoshida, S., Fujita, M., Mochizuki, M., Asada, A., 2011. Displacement above the hypocenter of the 2011 Tohoku-oki earthquake. Science 332, 1395.

Shao, G., Li, X., Ji, C., Maeda, T., 2011. Focal mechanism and slip history of the 2011 Mw 9.1 off the Pacific coast of Tohoku earthquake, constrained with teleseismic body and surface waves. Earth, Planets and Space 63, 559–564.

Shi, F., Kirby, J.T., Harris, J.C., Geiman, J.D., Grilli, S.T., 2012. A high-order adaptive time-stepping TVD solver for Boussinesq modeling of breaking waves and coastal inundation. Ocean Modelling 43–44, 36–51.

Simons, M., et al., 2011. The 2011 Magnitude 9.0 Tohoku-Oki earthquake: mosaicking the megathrust from seconds to centuries. Science 332, 1421–1425.

Stein, S., Geller, R.J., Liu, M., 2012. Why earthquake hazard maps often fail and what to do about it. Tectonophysics 562–563, 1–25.

Suyehiro, K., Sacks, I.S., Acton, G.D., Oda, M. (Eds.), 2003. Proceeding of the Ocean Drilling Program, Scientific Results 186 (http://www-odp.tamu.edu/publications/186_SR/186sr.htm).

Synolakis, C.E., Bardet, J.-P., Borrero, J.C., Davies, H.L., Okal, E.A., Silver, E.A., Sweet, S., Tappin, D.R., 2002. The slump origin of the 1998 Papua New Guinea tsunami. Proceedings of the Royal Society of London Series A 458, 763–789.

Takagawa, T., Tomita, T., 2012. Effects of rupture processes in an inverse analysis on the tsunami source of the 2011 Off the Pacific Coast of Tohoku earthquake. Proceedings of 22nd International Offshore and Polar Engineering Conference (ISOPE22), Rhodes, Greece, June 17–22, 2012. 3, pp. 14–19.

Tanioka, Y., Satake, K., 1996. Fault parameters of the 1896 Sanriku tsunami earthquake estimated from tsunami numerical modeling. Geophysical Research Letters 23, 1549–1552.

Tanioka, Y., Seno, T., 2001. Sediment effect on tsunami generation of the 1896 Sanriku tsunami earthquake. Geophysical Research Letters 28, 3389–3392. http://dx.doi.org/10.1029/2001GL013149.

Tappin, D.R., Watts, P., McMurtry, G.M., Lafoy, Y., Matsumoto, T., 2001. The Sissano Papua New Guinea tsunami of July 1998 — offshore evidence on the source mechanism. Marine Geology 175, 1–23.

Tappin, D., Watts, P., Grilli, S.T., 2008. The Papua New Guinea tsunami of 1998: anatomy of a catastrophic event. Natural Hazards and Earth System Sciences 8, 243–266.

Tappin, D.R., Evans, H.M., Jordan, C.J., Richmond, B., Sugawara, D., Goto, K., 2012. Coastal changes in the Sendai area from the impact of the 2011 Tōhoku-oki tsunami: interpretations of time series satellite images, helicopter-borne video footage and field observations. Sedimentary Geology 282, 151–174.

Tehranirad, B., Shi, F., Kirby, J.T., Harris, J.C., Grilli, S.T., 2011. Tsunami benchmark results for fully nonlinear Boussinesq wave model FUNWAVE-TVD, Version 1.0. Technical Report CACR-11-02. Center for Applied Coastal Research, University of Delaware.

Tomita, T., Yoem, G.-S., 2012. Tsunami damage in ports by the 2011 off Pacific coast of Tohoku earthquake. Proceedings of International Symposium on Engineering Lessons Learned from the 2011 Great East Japan Earthquake (March 1–4, 2012, Tokyo, Japan).

Tsuji, Y., Matsutomi, H., Imamura, F., Takeo, M., Kawata, Y., Matsuyama, M., Takahashi, T., Sunarjo, Harjadi, P., 1995. Damage to coastal villages due to the 1992 Flores Island Earthquake Tsunami. Pure and Applied Geophysics 144, 481–524.

Tsuru, T., Park, J.-O., Miura, S., Kodaira, S., Kido, Y., Hayashi, T., 2002. Along-arc structural variation of the plate boundary at the Japan Trench margin: implication of interplate coupling. Journal of Geophysical Research 107, 2,357. http://dx.doi.org/10.1029/2001JB001664.

Turner, A.K., Schuster, R.L., 1996. Landslides: Investigation and mitigation. Special Report 247. Transportation Research Board, National Academy Press, Washington, D.C.

von Huene, R., Klaeschen, D., Cropp, B., Miller, J., 1994. Tectonic structure across the accretionary and erosional parts of the Japan trench margin. Journal of Geophysical Research 99, 22,349–22,361.

Watts, P., Grilli, S.T., Kirby, J.T., Fryer, G.J., Tappin, D.R., 2003. Landslide tsunami case studies using a Boussinesq model and a fully nonlinear tsunami generation model. Natural Hazards and Earth System Sciences 3, 391–402.

Watts, P., Grilli, S.T., Tappin, D., Fryer, G.J., 2005. Tsunami generation by submarine mass failure Part II : Predictive Equations and case studies. Journal of Waterway, Port, Coastal and Ocean Engineering 131, 298–310.

Wei, G., Kirby, J.T., Grilli, S.T., Subramanya, R., 1995. A fully nonlinear Boussinesq model for surface waves. I. Highly nonlinear, unsteady waves. Journal of Fluid Mechanics 294, 71–92.

Wei, S.J., Graves, R.W., Helmberger, D., Avouac, J.P., Jiang, J.L., 2012. Sources of shaking and flooding during the Tohoku-Oki earthquake: a mixture of rupture styles. Earth and Planetary Science Letters 333–334, 91–100.

Wei, Y., Newman, A., Hayes, G., Titov, V., Tang, L., 2014. Tsunami forecast by joint inversion of real-time tsunami waveforms and seismic or GPS Data: application to the Tohoku 2011 tsunami. Pure and Applied Geophysics 1–25. http://dx.doi.org/10.1007/s00024-014-0777-z.

Yagi, Y., Fukahata, Y., 2011. Rupture process of the 2011 Tohoku-oki earthquake and absolute elastic strain release. Geophysical Research Letters 38. http://dx.doi.org/10.1029/2011GL048701 (L19307).

Yamazaki, Y., Lay, T., Cheung, K., Yue, H., Kanamori, H., 2011. Modeling near-field tsunami observations to improve finite-fault slip models for the 11 March 2011 Tohoku earthquake. Geophysical Research Letters 38. http://dx.doi.org/10.1029/2011GL049130 (L00G15).

Yamazaki, Y., Cheung, K.F., Lay, T., 2013. Modeling of the 2011 Tohoku near-field tsunami from finite-fault Inversion of seismic waves. Bulletin of the Seismological Society of America 103, 1444–1455.

Yue, H., Lay, T., 2011. Inversion of high-rate (1 sps) GPS data for rupture process of the 11 March 2011 Tohoku earthquake (Mw 9.1). Geophysical Research Letters 38. http://dx.doi.org/10.1029/2011GL048700 (L00G09).

Yue, H., Lay, T., 2013. Source rupture models for the Mw 9.0 2011 Tohoku earthquake from joint inversions of high-rate geodetic and seismic data. Bulletin of the Seismological Society of America 103, 1242–1255.